Mechano-electric coupling in P(VDF–TrFE)/spin crossover composites

Mario Piedrahita-Bello, Baptiste Martin, Lionel Salmon, Gábor Molnár, Philippe Demont, Azzedine Bousseksou

Mechano-electric coupling in P(VDF–TrFE)/spin crossover composites†

Mario Piedrahita Bello, [a] Baptiste Martin, [b] Lionel Salmon, *[a] Gábor Molnár, [a] Philippe Demont[b] and Azzedine Bousseksou*[a]

DOI: 10.1039/d0tc00780c

Spin crossover particles dispersed in a piezo/ferroelectric poly(vinylidene fluoride-co-trifluoro-ethylene), P(VDF TrFE), matrix give rise to inspiring mechano-electric phenomena, with possible applications for energy harvesting and sensing. Particles of different chemical compositions, morphologies and concentrations were loaded into copolymers with different TrFE molar contents to investigate the effect of these parameters on the mechano-electric coupling between the polymer and the spin crossover material. The samples were characterized by elemental analysis, powder X-ray diffraction, Raman spectroscopy, optical reflectivity, differential scanning calorimetry, and electron microscopy and were studied also for their piezo/pyroelectric properties. We show that it is possible to tune simultaneously the spin transition temperature of the particles and the Curie temperature of the matrix in such a way that the piezoelectric effect from the spin transition and the pyroelectric response of the polymer can be concomitantly observed. This result provides prospects for the development of smart, multifunctional electroactive polymer composites and for increasing their thermal electrical harvester output.

Introduction

Harvesting thermal and mechanical "waste" energy is a potentially powerful strategy to develop self-powered devices and to reduce overconsumption of fossil fuels.[1,2] In this area of research, various technologies have been developed incorporating piezoelectric, electromagnetic, electrostatic and triboelectric energy harvesters; the piezoelectric mechanism being the most common.[3,4] These devices use the piezoelectric properties of certain materials, *i.e.* they produce electric charges when stimulated by a mechanical stress. Some of the popular materials, which exhibit piezoelectricity, are lead zirconate titanate, barium titanate, lithium niobate, aluminium nitride, zinc oxide and polyvinylidene fluoride (PVDF) as well as its copolymers. Since many of these materials display pyroelectric properties as well, they allow also the conversion of temperature fluctuations into electrical energy.[5,6] However, the limited choice of piezo/pyro-electric materials and complex fabrication techniques still represents an important challenge. One of the strategies to overcome these limitations and to increase the efficiency of the harvester output involves developing composite and nanocomposite materials.[7]

[a] *LCC, CNRS & University of Toulouse (UPS, INPT), 205 route de Narbonne, 31077 Toulouse, France. E mail: azaedine.bousseksou@lcc toulouse.fr, lionel.salmon@lcc toulouse.fr*

[b] *CIRIMAT, CNRS & University of Toulouse (UPS, INPT), 118 Route de Narbonne, 31062 Toulouse, France. E mail: philippe.demont@univ tlse3.fr*

Notably, an interesting approach aims at combining a pyroelectric compound with another material, which exhibits large thermal strains (*e.g.* thermal expansion or phase transition). Since all pyroelectric materials are piezoelectric as well, the strain in the second component gives rise to an electrical voltage or current in the first component – provided that they are mechanically coupled.[5] The efficiency of this approach was, for example, demonstrated using a PVDF/TiNiCu (shape memory alloy) composite, which allowed, under specific conditions, the enhancement of the intrinsic pyroelectric response of PVDF by the piezoelectric effect.[8]

In this context, molecular spin crossover (SCO) materials exhibiting large thermal strains appear particularly appealing. These transition metal complexes display a reversible switching between the low spin (LS) and high spin (HS) states upon heating/cooling, which is accompanied by a substantial volume change of the crystal lattice (up to 10–15% in certain compounds).[9–11] Recently, we[12] and others[13] reported on the synthesis of composite materials wherein electroactive polymers were loaded with SCO particles. The initial objective of these studies was to endow the SCO composite material with unprecedented electrical properties through the mechano-electric coupling between the particles and the matrix. Notably, Koo *et al.*[13] incorporated the SCO compound $[Fe(Htrz)_2(trz)](BF_4)$ (Htrz = 1*H*-1,2,4-triazole, trz- = 1,2,4-triazolato) in a piezoresistive polypyrrole matrix, affording a semiconducting composite, which displayed bistability of its conductivity.[13] In our group, we have synthesized a composite material combining the ferroelectric polymer P(VDF–TrFE) with

the SCO complex $[Fe(Htrz)_{1.85}(trz)_{0.85}(NH_2trz)_{0.3}](BF_4)_{1.15}\cdot H_2O$ (NH_2trz = 4-amino-1,2,4-triazole).[12] When heated or cooled, the composite exhibited a current discharge around the spin transition temperatures. We attributed this phenomenon to the effective coupling of the SCO-induced strain to the piezoelectric matrix. An interesting possible application of this property would be thermal energy harvesting. However, the composite reported in ref. 12 did not display notable pyroelectric properties.

In this paper, we report on the elaboration of a series of P(VDF–TrFE)–SCO nanocomposites, while varying the composition of the polymer as well as the composition, the concentration and the morphology of the spin crossover particles. Our aim is to show that by tuning the matrix and particle properties it is possible to observe concomitantly the piezoelectric effect from the spin transition and the pyroelectric response of the polymer.

Among the available ferroelectric polymers, we use P(VDF–TrFE) copolymers, which are attractive for their good piezo- and pyroelectric responses as well as for their easy and versatile processing.[14] The use of copolymers instead of the pure PVDF is an effective method to tune the polymer structure and to increase the proportion of the ferroelectric β phase, which is attributed to the steric hindrance effect of the bulky co-monomer TrFE. Nevertheless, an additional thermal annealing process is generally used to increase the degree of crystallinity and a further high voltage poling is necessary to align the ferroelectric domains. On the other hand, composites and nanocomposites have been also developed in order to increase the proportion of the β phase. The influence of the particles on the piezoelectric properties of the composite depends on their size, shape, charge, surface chemistry, concentration and dispersion.[14]

The choice of the SCO complex is imposed by the temperature window wherein the polymers can be conveniently used, *i.e.* between the so-called α-relaxation near-room-temperature, which corresponds to the glass transition, and the Curie transition, which occurs at higher temperatures and corresponds to the first-order transition between the ferroelectric β phase and the paraelectric α phase.[15] Notably, P(VDF–TrFE) with 70–30 mol% monomer ratio, which was used in ref. 12, displays a Curie point at 105 °C, whereas for 75–25 mol% the Curie point shifts to 115 °C. The latter co-polymer, despite being slightly less piezoelectric, appears thus more interesting for our work as it provides a broader 'temperature window' for the choice of the SCO complex.

Indeed, numerous SCO materials are known to display spin transition in this 'temperature window'.[9] In our study we used the one-dimensional coordination networks of $[Fe(Htrz)_{1+y-x}(trz)_{2-y}(NH_2trz)_x](BF_4)_y\cdot nH_2O$ showing thermal spin transitions between *ca.* 50 °C and 100 °C (depending on the stoichiometry) as well as the mononuclear complex $[Fe(HB(tz)_3)_2]$ (tz = 1,2,4-triazol-1-yl) presenting a very stable abrupt spin transition around 60 °C. It is worth noting that the spin transition is first-order in each compound and is therefore accompanied by a thermal hysteresis loop (see Fig. 1 and Table 1 for more details on the SCO samples).

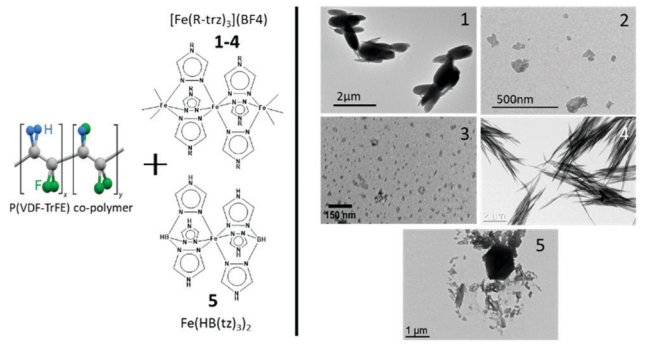

Fig. 1 Chemical structure of the polymer matrix and the SCO complexes used. TEM images of the different SCO materials (**1–5**).

Experimental section

Synthesis of the SCO samples

All the chemicals and solvents were obtained from Sigma Aldrich and used without any further purification. The microcrystalline powder sample 1 was obtained using the following procedure: 7.5 ml of a 0.395 M solution of $Fe(BF_4)_2\cdot 6H_2O$ was mixed with a solution containing a mixture of 50 mg of 1,2,4-4-NH_2-triazole (6.6%) and 572 mg of 1,2,4-4-*H*-triazole. The mixture became pink after a minute and was allowed to react for 12 h. The resulting pink solid was cleaned multiple times by centrifugation with ethanol and dried under vacuum. The nanoparticle sample **2** is the same synthesis batch, which was described in ref. 12. Compound **3** is a similar nanoparticle sample, with slightly different stoichiometry, which was described in ref. 16. Rod-like microparticles (compound **4**) were prepared using the following procedure: two equivalent microemulsions were prepared mixing together 3.85 ml of Triton X-100, 3.6 ml of pentanol and 8 ml cyclohexane. To this mixture, a solution of 424 mg of $Fe(BF_4)_2\cdot 6H_2O$ in 2.75 ml H_2O was added dropwise to obtain the first microemulsion, whereas a solution of 234 mg of 1,2,4-4-*H*-triazole and 32 mg of 1,2,4-4-NH_2-triazole (6.6%) in 2.75 ml H_2O was added to obtain the second microemulsion. These microemulsions were stirred at room temperature until clear solutions were obtained and then

Table 1 Composition, morphology and spin transition temperatures (upon heating and cooling) of the SCO complexes used

SCO sample	Composition	Morphology	$T_{SCO}\uparrow$ (°C)	$T_{SCO}\downarrow$ (°C)
1	$[Fe(Htrz)_{1,85}(trz)_{0,95}(NH_2trz)_{0,2}](BF_4)_{1,05}\cdot 0.6H_2O$	Microcrystalline	84	62
2	$[Fe(Htrz)_{1,85}(trz)_{0,85}(NH_2trz)_{0,3}](BF_4)_{1,15}\cdot 1H_2O$	20 nm particles	65	57
3	$[Fe(Htrz)_{2.05}(trz)_{0.75}(NH_2trz)_{0.2}](BF_4)_{1.25}\cdot 1H_2O$	20 nm particles	73	58
4	$[Fe(Htrz)_{1.8}(trz)_1(NH_2trz)_{0.2}](BF_4)_1\cdot 0.7H_2O$	2 μm rods	91	71
5	$[Fe(HB(tz)_3)_2]$	Microcrystalline	63	62

quickly mixed together. Several minutes after, the mixture became pink due to the particle formation. The resulting microemulsion was agitated for 24 hours to ensure that the microemulsion exchange was completed. Then, 30 ml ethanol was added to destroy the microemulsion structure. The obtained nanoparticles were washed several times with ethanol to remove the traces of the surfactants and separated by centrifugation (4000 rpm, 10 minutes). The microcrystalline powder sample **5** was obtained according to ref. 17. The composition of the non-stoichiometric samples **1–4** was established thanks to combined C, H, N, B, and Fe elemental analyses (see Table 1 and ESI,† Table S1). The theoretical quantity of the elements was calculated with respect to the $[Fe(Htrz)_{1+y-x}(trz)_{2-y}(NH_2trz)_x](BF_4)_y \cdot nH_2O$ formula.

Elaboration of the nanocomposite films

The P(VDF–TrFE)/SCO composites were prepared by dispersing each SCO complex (90 mg) in 2-butanone (1.8 ml) in an ultrasonic bath for 40 min. Then, the corresponding PVDF–TrFE copolymer (270 mg) was added to the mixture and dissolved at 45 °C. The resulting suspensions were then blade-cast at a height of 150 μm on a heated Teflon surface at 50 °C and kept at this temperature for *ca.* 2 h, until the composite was completely dry (Fig. 2). The films were then annealed at 105 °C for 12 h.

Sample characterization

Variable temperature powder X-ray diffraction (PXRD) patterns of the samples have been recorded using a Panalytical MPD X'PertPro diffractometer [CuKα1, Ge(111) monochromator, X'Celerator detector] within the range of 5–50° (2θ) at a scan speed of 30° per hour. Scanning electron microscopy (SEM) images were acquired in a secondary electron mode using a JEOL JSM 7800F Prime operated at 5 kV. Samples for SEM were prepared by breaking the film and the cross-section was metalized with Pt. The particle morphology of the SCO powders was investigated by transmission electron microscopy (TEM) using a JEOL JEM-1011. TEM samples were prepared by placing on a carbon-coated copper grid a drop of the particles suspended in ethanol. Variable-temperature optical reflectivity data were acquired with a MOTIC SMZ-168 stereomicroscope equipped with a MOTICAM 1000 color CMOS camera. A 2 K min^{-1} rate was used for both cooling and heating. Variable temperature Raman spectra were acquired using an Xplora (Horiba) Raman microspectrometer (resolution *ca.* 3 cm^{-1}). The 532 nm line of a Nd-YAG laser (0.1 mW) was focused on the sample by a ×50 objective (numerical aperture, NA = 0.5), which was also used to collect the backscattered photons. Differential scanning calorimetry (DSC) analysis was carried out on a Netzsch DSC 204 instrument under helium purging gas. The measurements were conducted between 0 and 250 °C at a scan rate of 10 K min^{-1} both on heating and cooling. The temperature and enthalpy were calibrated using the melting transition of standard materials (Hg, In, and Sn). Elemental analyses of C, H, and N were performed by means of a PerkinElmer 2400 series II device after combustion at 850 °C, using IR detection and gravimetry. Elemental analyses of Fe and B were carried out using a Thermo Scientific ICAP 6300 inductively coupled plasma atomic emission spectrometer (ICP-AES).

The composites and the pure polymer reference samples were poled at room temperature using an Agilent 33220A waveform generator and a Trek high voltage amplifier. Several cycles of a sinusoidal poling electric field up to 60 MV m^{-1} were applied at a frequency of 100 mHz. During poling, the samples were immerged in silicon oil to prevent arcing. Piezoelectric strain coefficient d_{33} was measured 24 h after the poling step, using a PM 200 piezometer supplied by Piezotest (UK), with a strength of 0.25 N at 110 Hz frequency. Pyroelectric current measurements were performed using a Setaram TSCII instrument. The composite samples were short-circuited between two 1 cm diameter circular stainless-steel electrodes and through a Keithley 6517A electrometer and cycled with heating and cooling rates of 2 K min^{-1} (unless otherwise stated) between 293 and 365 K under a helium atmosphere.

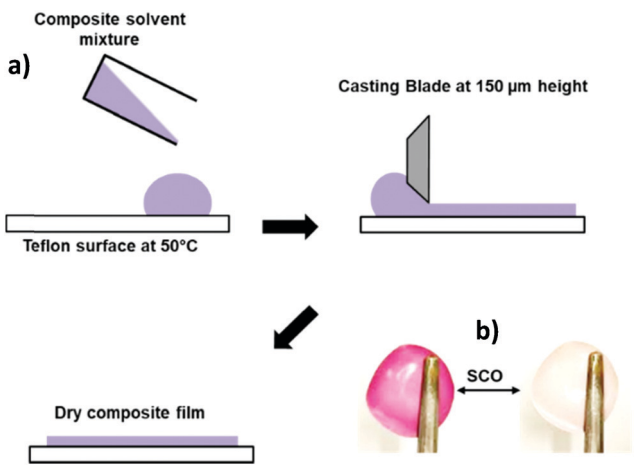

Fig. 2 (a) Scheme of the preparation of the P(VDF TrFE)/SCO composite films and (b) thermochromism of the composite film **5b**.

Results and discussion

Sample optimization

Fig. 1 and Table 1 summarize the properties of the five SCO complexes used in this work. Briefly, complexes **1–4** correspond to the same family of compounds, direct derivatives of the benchmark SCO complex $[Fe(Htrz)_2(trz)](BF_4)$. In order to adjust the spin transition temperature the trz ligand was partially substituted with small amounts of NH_2trz as described in ref. 18. In order to modulate the morphology of the particles, different synthesis techniques were used. Small (*ca.* 20 nm) particles were obtained using supersaturated solutions (samples **2–3**).[16] Rod shaped particles (*ca.* 2 μm long) were synthesized using reverse micelles as nanoreactors (sample **4**). Complexes **1** and **5** were obtained as microcrystalline powders.

Composite films were obtained by dispersing the SCO powders with adequate P(VDF–TrFE) co-polymers in 2-butanone and casting them on a Teflon surface. A casting blade was used to control the height of the deposit (see Fig. 2). A last annealing step renders the film crystalline. Finally, flexible, stable, freestanding films were peeled away from the Teflon substrate.

The principal challenge was to maximize the charge of the composite, while retaining sample homogeneity and good mechanical properties. Homogeneity and mechanical stability are essential both for sample poling and for the potential use of these materials for electromechanical applications. On the other hand, maximizing the proportion of the SCO complex obviously allows us to enhance the effects of the spin transition on the composite. This sample optimization required the control of several parameters such as the dispersion of the SCO complex in the polymer, the nature of the solvent, the concentration of the active spin crossover compound, the annealing temperature and the thickness of the film and led to multiple synthesis attempts. In particular, we observed that for a high SCO load, the composite becomes inhomogeneous and brittle, with very poor mechanical properties. A maximum load of *ca.* 15–33 wt% could be reached, depending on the SCO sample used, while keeping a good sample quality. Different dispersion methods were also tested: mixing the particles with the dissolved polymer under stirring, grinding the particles along with the polymer in a mortar and eliminating bubbles by drying the composite in a vacuum. The best results were obtained by sonication of the particles in an appropriate solvent before the addition of the polymer. We also examined different film thicknesses. Films under 50 μm, despite being highly homogeneous, were too fragile to be properly poled. We found a thickness of *ca.* 100 μm as a good compromise to obtain homogenous samples, which could be easily handled. The crystallization temperature from the solvent cast plays a crucial role in the electrical properties of the polymer.[19] An annealing temperature of 105 °C was found to be optimal for the crystallization of the β phase. It was under these considerations that we settled the synthesis conditions, as a means to optimize the different material properties. Overall, nine composite samples were prepared (see Table 2) allowing us to study the influence of the concentration, composition and morphology of the particles as well as the composition of the polymer.

Representative SEM images of composites **1a**, **2a**, **4a** and **5c** are shown in Fig. 3 and Fig. S1–S6 in the ESI.† The samples were chosen to highlight how different particle morphologies are dispersed in the polymer matrix. For composite **1a**, as expected for the bulk compound, inhomogeneous, aggregated objects contrast with the polymer fibres of the matrix. In the case of **2a**, the small particles form small aggregates attached to the polymer fibres. In composite **4a** the micrometric rods are clearly visible within the polymer matrix. Finally, in composite **5a** the contrast can be clearly seen between the micron-sized, rectangular particles and the much smaller polymer fibres.

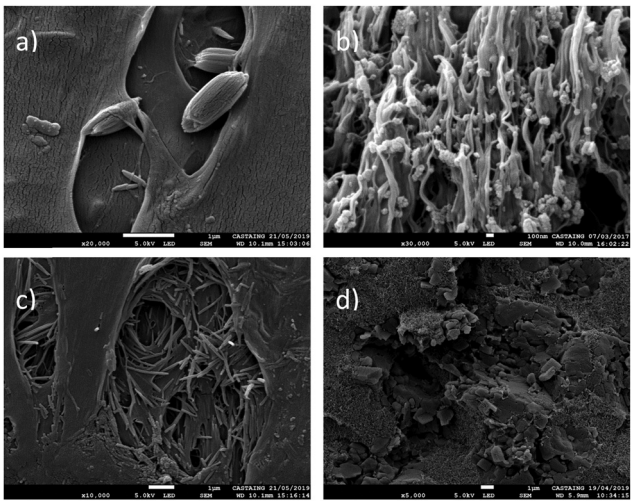

Fig. 3 Selected SEM images of the composite cross sections. (a) **1a**, (b) **2a**, (c) **4a** and (d) **5c**.

Table 2 Composition and properties of the composite and the pure polymer samples

Composite	SCO sample	Load wt%	VDF : TrFE (mol%)	d_{33} pCN^{-1}	Polarization field (MV m^{-1})
1a	**1**	15%	75 25	−13	27
2a	**2**	25%	70 30	−9	24
3a	**3**	15%	75 25	−15	39
4a	**4**	15%	75 25	−6.3	22
5a	**5**	33%	75 25	−4.5	40
5b	**5**	25%	70 30	−7.5	18
5c	**5**	25%	75 25	−6.5	21
5d	**5**	15%	75 25	−15	33
5e	**5**	5%	75 25	−19	49
PVDF TrFE	N/A	N/A	75 25	−19	54
PVDF TrFE	N/A	N/A	70 30	−20	57

β phase in the composite co-polymer

The proportion of the polar β phase in the polymer matrix depends on the experimental conditions and the nature of the filler. Raman spectroscopy, powder X-ray diffraction and differential scanning calorimetry were used to analyse the presence of this phase, the crystallinity of the samples and their Curie temperature. It should be noted that the decrease of the TrFE monomer fraction from 30 to 25% leads to the decrease of the proportion of the β phase.

The Raman spectra of the composites were found to be spatially homogenous, indicating good dispersion. They consist of the superposition of the spectra of the SCO compound and the P(VDF–TrFE) co-polymer (see Fig. 4). It is well-established that the β phase of the P(VDF–TrFE) matrix can be clearly discerned in the Raman spectrum at 840 cm^{-1} (850 cm^{-1} for the 70–30 copolymer), whereas the signature of the α phase appears at around 800 cm^{-1}.[20] Using these characteristic Raman peaks the proportion of the α and β phases can be estimated. The pure polymer with a 75 : 25 monomer ratio appears to be a mixture of the two phases, with a majority of β form. In the case of composites **1a** and **3a** the addition of the microcrystalline particles seems to have no substantial influence on the proportion of the β phase in comparison with the pure polymer. In the case of the other composites, the proportion of the β phase appears even higher than in the pure polymer, close to 100%, suggesting that the introduction of the particles favours the formation of the β phase. This result is in agreement with the PXRD data for the series of composites **5a**, **5c**, **5d** and **5e**, which are composed of the same SCO powder and co-polymer, but in different proportions (see Fig. S7 in the ESI†). In this series of composites, we can thus carry out a

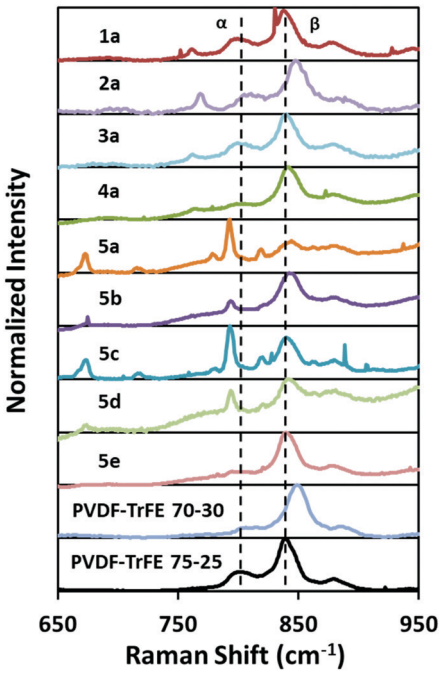

Fig. 4 Raman spectra of the composites and the pure polymers.

quantitative analysis of the relative intensities of the marker peaks of the SCO compound (at 2θ = 15.8°, 16.8°, 19.5° and 30.2°) and that of the β phase of the copolymer (at 2θ = 20.0°). It turns out that, within the experimental uncertainty, this ratio is proportional to the nominal load of the SCO particles. This means that these composites have similar crystallinity and contain similar amounts of the β phase.

DSC measurements performed on the different composites allow evidencing the spin transition, the para–ferroelectric phase transition and melting phenomena in a more quantitative manner (see Fig. 5 and Fig. S8 in the ESI†). The central issue here is that for the majority of the samples we were able to achieve a good separation between the spin transition and Curie peaks in the heating mode (see Table 3 and Fig. 5). This property is essential, because it allows one to run thermal cycles through the spin transition without affecting the β phase, which would be detrimental for the piezo/ferroelectric properties and thus the sample polarization. We stress that the DSC analysis was performed for the first thermal cycle of the samples. This is necessary because the LS to HS transition in some of the investigated complexes occurs at a slightly higher temperature on the first heating. (The shift of the first heating transition is well-known for many SCO materials and can be attributed to various phenomena such as the loss of solvents and/or particle morphology changes and/or polymorphism.[21,22])

It is important to remark also that taking an SCO complex with a spin transition temperature below the Curie point of the chosen copolymer does not necessarily ensure the separation of the two phenomena in the composite. The reason for this is that the SCO behaviour may change upon confinement in the polymer matrix and, likewise, the phase stability of the polymer can be affected by the filler. The latter phenomenon can be

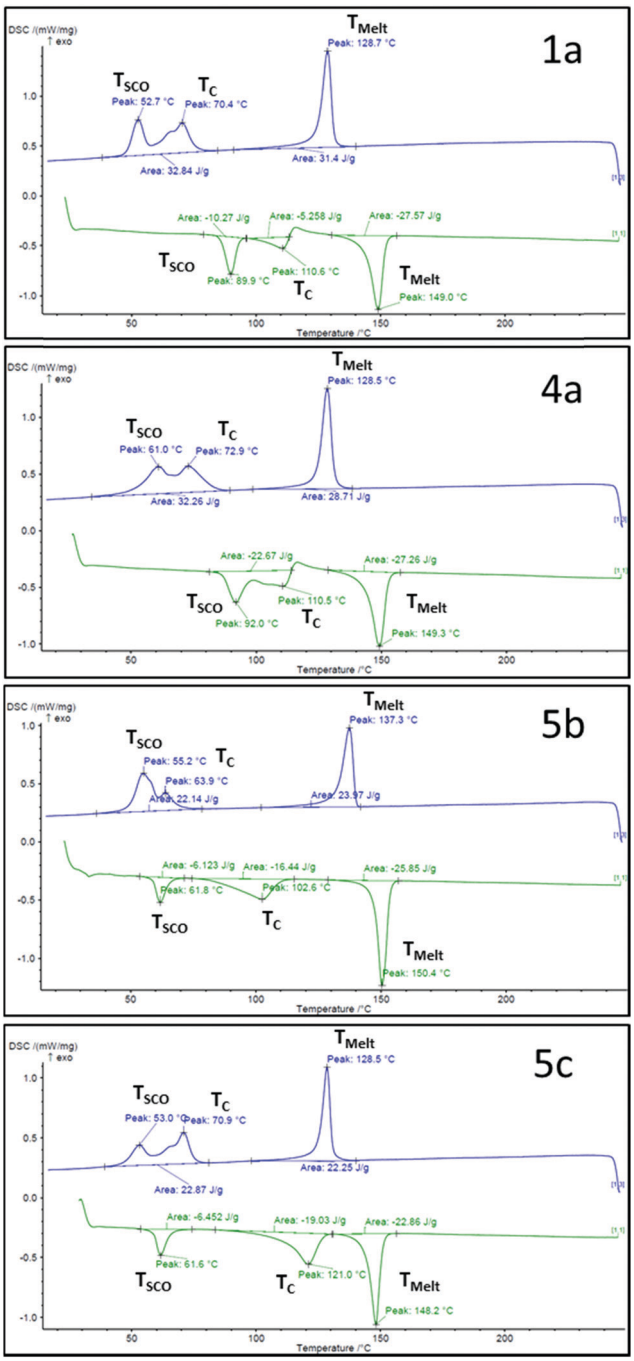

Fig. 5 DSC thermogram of composites **1a**, **4a**, **5b** and **5c**.

clearly seen in the case of composite **5a**, whose Curie temperature suffers a very significant downshift with respect to composites **5c**–**5e**, which have exactly the same chemical composition, but contain a smaller amount of filler. On the other hand, the SCO temperature does not change much in this series of composites, in contrast to the SCO compounds **1**–**4**, which exhibit a more pronounced matrix effect and, *vice versa*, they have a more pronounced impact on the para/ferroelectric transition temperature as well. The DSC data allow also for an estimation of the crystallinity of the polymer matrix, which is considered

Table 3 DSC data for the composite and pure polymer samples

	T_{SCO} (°C)		T_{Curie} (°C)		$T_{melting}$ (°C)				
Sample	Heating	Cooling	Heating	Cooling	Heating	Cooling	ΔH_{Curie} (J g^{-1})	$\Delta H_{melting}$ (J g^{-1})	Crystallinity (%)
1a	90	53	110	70	149	129	29	32	65
2a	60	44	100	57	150	135	17	28	49
3a	86	53	111	71	149	129	25	29	58
4a	92	61	110	73	149	128	29	32	65
5a	64	52	104	62	152	136	21	34	59
5b	62	55	103	64	150	137	19	34	58
5c	62	53	121	71	148	129	20	30	54
5d	61	53	122	70	149	129	25	36	65
5e	61	54	123	71	149	129	19	33	56
75 25	N/A	N/A	111	75	143	129	11	24	38
70 30	N/A	N/A	105	62	149	129	13	29	46

proportional to the enthalpy variation measured taking into account both the Curie and melting transitions.[15,23] Interestingly, the crystallinity of each composite is higher than that of the corresponding pure polymer in particular for the copolymers, P(VDF–TrFE) 75–25% (Table 3). On the other hand, the latent heat associated with the para/ferroelectric transition provides information on the (relative) proportion of the β phase in the different samples. Due to the difficulties in properly determining the baseline of the DSC thermograms, the experimental uncertainty is higher here. Nevertheless, we find values of latent heat around 23 ± 6 J g^{-1} (corrected for the polymer content) (Table 3). While the relationship between load and crystallinity so far remained unclear, there is a tendency not only for higher crystallinity, but also for a higher proportion of the β phase in the composites – in particular in samples **1a**, **3a** and **4a**.

Spin crossover properties and matrix effect

To further investigate the effect of the matrix on the SCO properties variable-temperature optical reflectivity measurements were carried out on the different powders and polymer composite materials (see Fig. 6 and Fig. S9, S10 in the ESI†). Due to the strong optical contrast between the HS and LS forms, this technique allows us to acquire in a straightforward manner the thermally induced SCO curves. The spin transition temperatures for the second (stable) cycle are gathered in Table 4. As it was already observed for composite **2a**,[12] the SCO hysteresis width in each composite is noticeably increased, in comparison with that of the corresponding neat powder sample, though the changes are less pronounced for the [Fe(HB(tz)$_3$)$_2$] composites **5a–5e**. Based on recent theoretical works,[24]

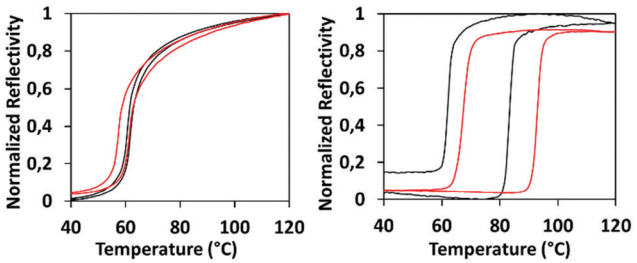

Fig. 6 Variable temperature optical reflectivity measurements for the bulk compounds **1** and **5** (in black) and the corresponding composite samples **1a** and **5a** (in red).

Table 4 Spin transition temperatures of the neat SCO complexes and their corresponding polymer composites obtained by optical reflectivity. (All data correspond to the second thermal cycle. $T\uparrow$ and $T\downarrow$ stand for the transition temperature on heating and cooling respectively. $\Delta T = T\uparrow - T\downarrow$)

	Bulk powder			Composite		
Sample	$T\uparrow$ (°C)	$T\downarrow$ (°C)	ΔT (°C)	$T\uparrow$ (°C)	$T\downarrow$ (°C)	ΔT (°C)
1	84	62	22	94	67	27
2	65	57	8	67	54	13
3	73	58	15	83	58	25
4	91	71	20	95	69	26
5	63	62	1	62	57	5

we suggest that these changes of SCO properties arise presumably due to the elastic confinement of the matrix, though other reasons (*e.g.* reduced heat conduction or solvent effects) cannot be excluded either.

Mechano-electric coupling in the composites

In order to align the ferroelectric domains and observe a non-zero macroscopic polarization, the composite samples as well as the pure polymers were poled under a strong electrical field. It should be noted that, depending on the homogeneity of the composite film, the polarization field could cause breakage of the material. For this reason, for each composite film there is a maximum level of polarization field it can be subjected to and a corresponding piezoelectric coefficient d_{33}. These values are gathered in Table 2 for the different samples. Poling of the composite samples was undertaken at 293 K with amplitudes ranging from 2 to 50 MV m^{-1}. The resulting piezoelectric coefficient d_{33}, which provides direct information on the mechanical to electrical (and *vice versa*) conversion efficiency, spans from −4.5 to −19.0 pC N^{-1} for the composites. As it can be expected, the piezoelectric coefficient has reduced values with respect to those of the pure polymers (*ca.* −19–20 pC N^{-1}). This is an obvious effect in P(VDF–TrFE) composites with non-ferroelectric fillers[25] and can be attributed to the reduced volume fraction of the polymer as well as to the increasing sample heterogeneity, which leads to the reduction of the maximum polarization field (from *ca.* 55 MV m^{-1} in the pure copolymers to *ca.* 20 MV m^{-1} in some of the composites) before breakdown occurs. It is interesting to note that in some cases it was possible to maintain a piezoelectric coefficient that is not far from that of the pure

polymer even for particle loads of 15%. On the other hand, the further increase of the load is concomitant with the inevitable decrease of the d_{33} coefficient.

The spin transition in compounds **1–4** and **5** is associated with a substantial spontaneous volumetric strain of *ca.* 10% and 4.5%, respectively.[17,26] If this mechanical strain is efficiently transferred to the electroactive polymer matrix a change in the polarization level of this latter should take place due to the electro-mechanical coupling. Under short-circuit conditions, one would therefore expect a transient current flow during the spin transition. This phenomenon has been demonstrated in our previous publication using the composite sample **2a**.[12] As mentioned before, in the present work we aimed at investigating the versatility of this approach through the series of composites **1a–5e**. In particular, we seek for the possibility of tuning simultaneously the properties of the polymer and the SCO filler – by modulating their composition, concentration and microstructure – in such a way that the pyroelectric effect of P(VDF–TrFE) and the piezoelectric effect due to the SCO appear concomitantly in the composite.

To investigate this issue, each composite was first poled and then thermally cycled (without any applied voltage) to measure the current discharged upon heating and cooling. Fig. 7 shows the short-circuit current measurements for the composite series **5a–5e** (see also Fig. S15–S22 in the ESI†). For loads of 5% (**5e**) and 15% (**5d**), the pyroelectric current in the composites remains virtually unchanged in comparison with that of the pure polymer matrix. This finding is in agreement with the relatively high piezoelectric coefficients d_{33} of these composites (Table 2). In other words, for this concentration range, the piezoelectric properties of the composites correspond very closely to that of the pure polymer. This result proves the successful separation of the temperature regions in which the spin transition and ferro/paraelectric transition occur. In addition to the conventional pyroelectric behavior, a small discharge peak is also discernible at the spin transition temperature even at relatively low filler concentrations. However, the intensity of these peaks remains weak. These "weakly charged" (<15%) composites of compound **5** can be therefore considered, from an electrical point of view, nearly equivalent to the pure polymer. At the same time, however, the introduction of the SCO filler gives rise to interesting new, smart functionalities, such as pronounced thermochromism (see Fig. 2) and paramagnetism (in the HS state), which are obviously not present in the neat polymer and which can enlarge therefore the scope of its applications.

On the other hand, the presence of the discharge peaks associated with the spin transition can be considered as an electrical signature of the SCO, which is also a new property,

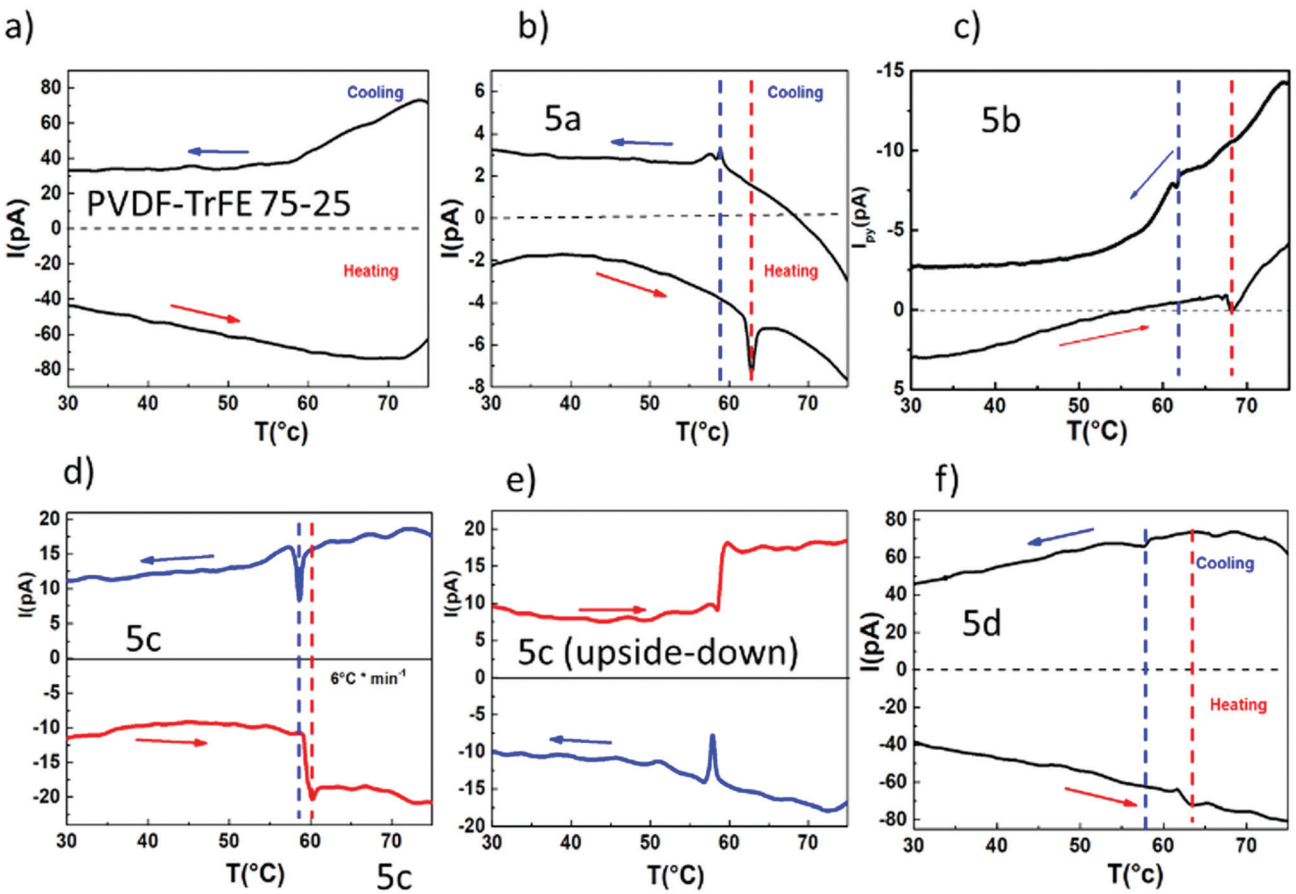

Fig. 7 (a) Pyroelectric discharge cycles for the pure 75 25% P(VDF TrFE) polymer. (b f) Pyroelectric discharge cycles for composites **5a–5d**. The arrows indicate heating and cooling. Dotted lines show the SCO related discharge peaks for cooling (left) and heating (right).

since SCO materials are, in general, nearly perfect dielectrics. In this context, it is interesting to note that most of the samples display SCO-related discharge peaks even in the absence of polarization. As an example, Fig. S18 in the ESI† shows the pyroelectric discharge cycle for the non-poled compound **5d**, wherein weak intensity, but clearly discernible peaks appear at the spin transition temperatures upon heating and cooling. As it could be expected, for increasing SCO content (samples **5a–5c**) the discharge peaks associated with the spin transition appear more clearly. In reality, this observation is not linked to a substantial increase of the discharge current at the SCO. Instead, the peaks emerge because the conventional pyroelectric response (*sic* "the baseline") shrinks drastically (see Fig. 7b–d) leading to a much lower electrical yield. It is interesting to compare the pyroelectric discharge cycles of composites **5b** and **5c**, which were synthesized with the same load (25%), but using the two different copolymers, P(VDF–TrFE) 70–30% and 75–25%, respectively. Owing to the better separation between the spin transition temperature and the Curie temperature, sample **5c** exhibits discharge peaks upon spin transition with higher intensity. In addition, one can observe a more characteristic pyroelectric behavior with a clear inversion of the polarity of the pyroelectric current between heating and cooling and also when returning the sample (Fig. 7d and e). This co-existence of the pyro- and piezoelectric phenomena stems obviously from the very neat separation between the spin transition and Curie temperatures in this sample (Fig. 5).

Another important comparison can be made between sample **5b** (Fig. 7c) and the previously published sample **2a** (Fig. S12, ESI†), which were made using the same copolymer and the same load (25%), but using two different SCO compounds. There is indeed a striking decrease of the intensity of the SCO-related discharge peaks in **5b**, based on compound $[Fe(HB(tz)_3)_2]$, when compared to **2a**, based on the Fe-triazole chains. We believe that this difference can be attributed primarily to the fact that the volume change for the $[Fe(HB(tz)_3)_2]$ complex upon the spin transition is significantly lower, *ca.* 5%,[17] when compared to that of complexes **1–4** with formulae $[Fe(Htrz)_{1+y-x}(trz)_{2-y}(NH_2trz)_x](BF_4)_y \cdot nH_2O$, which present up to 10% volume change.[26]

Fig. 8 gathers the key results obtained for composites **1a–4a** with the Fe-triazole family SCO complexes (see also Fig. S11–S14 in the ESI†). Composite **4a** appears singular in this series of samples, as it displays neither pyro-electricity nor SCO-related discharge peaks. Indeed, this sample was particularly difficult to polarize (see Table 2). In addition, in composite **4a** the spin transition in the first heating cycle strongly overlaps with the Curie transition leading eventually to the destruction of the (weak) polarization achieved. It can be suggested that the needle-shaped particles are disadvantageous in terms of the resistance to high, applied electrical fields, due to the existence of sharp points within the dielectrics, which may lead to localized electrical discharges and treeing. Furthermore, the anisotropy of the particles,

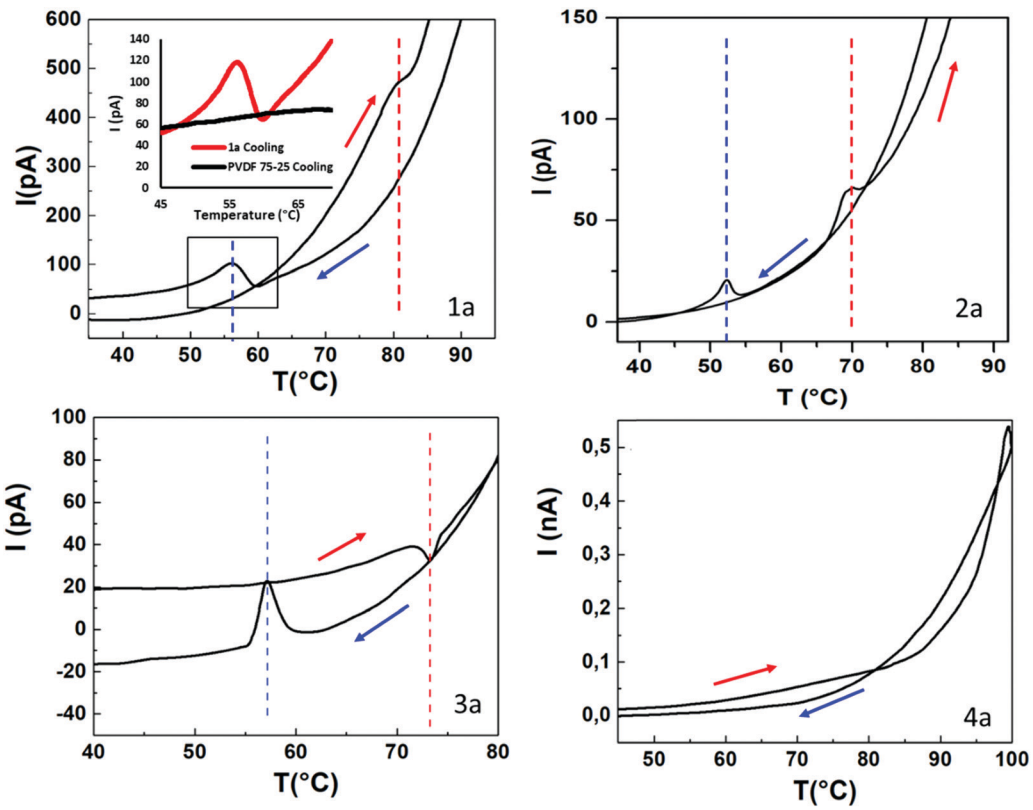

Fig. 8 Pyroelectric discharge cycle for the polarized samples **1a–4a**. The arrows indicate heating and cooling. Dotted lines show the SCO related discharge peaks for cooling (left) and heating (right). The inset shows a comparison between sample **1a** and pure PVDF TrFE 75 25 (current corrected for the amount of polymer).

which are mostly oriented in plane, is also unfavorable because most of the SCO-related strain is produced perpendicular to the polarization direction. These effects are effectively reduced in composites **1a–3a**, which can be therefore more efficiently polarized and which should provide also an increased strain component in the polarization direction. Yet, the use of the 70–30% P(VDF–TrFE) matrix in sample **2a** presents inconvenience due to the lower Curie temperature, which is overlapped with the spin transition, resulting in the (partial) erasing of the polarization during the thermal cycles. This problem was considerably reduced using the 75–25% P(VDF–TrFE) matrix, which allowed us to observe a suitable pyroelectric current (inversion of polarity upon heating and cooling) for samples **1a** and **3a**. In addition, the SCO-related discharge peaks reach also remarkable amplitudes in these samples, to such an extent that within a restricted range of temperatures around the SCO, the pyroelectric discharge is more intense for composite **1a** than for pure PVDF–TrFE 75–25 (Fig. 8, inset).

Overall, these results provide clear proof for the possibility of combining the pyroelectric response of the polymer with the piezoelectric effect arising due to the SCO. Nevertheless, to exploit this combined effect for thermal energy harvesting the following issues will have to be considered. First, a real gain with respect to state-of-the-art pyroelectric harvesters can be expected only for small and slow temperature excursions around the spin transition temperature. Second, the ideal SCO compound should display a relatively abrupt spin transition without hysteresis in the temperature range between *ca.* 30 and 50 °C and an associated large volume change (*ca.* 10%). Third, it is obviously important to find an arrangement where the sign of the two effects (pyro and piezo) are such that they sum up and not cancel each other. Indeed, in our different samples we observed both situations (see for example Fig. 7b and d). This means that different effects are in competition within the material. Notably, since the pyroelectric coefficient is negative, and upon heating the SCO material exhibits tensile strain (expansion) the two effects will sum up only if the piezoelectric coefficient has a positive sign. Since in P(VDF–TrFE) $d_{33} < 0$ whereas d_{31}, $d_{32} > 0$, various situations may arise depending on the effective anisotropy of the SCO strain. Besides, other phenomena may also contribute to the piezoelectric response, such as the variation of the dielectric permittivity upon the SCO (Fig. S23, ESI†). Material and mechanical engineering must consider these effects in order to optimize the harvesting output.

Conclusions

In summary, this work allowed us to demonstrate that the mechano-electric coupling between a ferroelectric P(VDF–TrFE) copolymer matrix and spin crossover particles, revealed in our previous communication,[12] is a generic property, which could be reproduced here for a series of composites containing different SCO compounds with different particle concentrations and morphologies. The key result of the present work is that by tuning the Curie temperature of the copolymer (*via* the modification of the VDF : TrFE ratio) and the spin transition temperature of the particles we were able to effectively separate these two phenomena and recover thus the pyroelectric property of the neat polymer. Depending on the concentration of the SCO filler, we observed two behaviors. In the low-concentration limit (*ca.* 5–15% – depending on the experimental details), we were able to achieve electromechanical properties in the composites, which are comparable with those of the pure polymer matrix. These composites can be considered as high performance, multifunctional, smart materials displaying interesting electromechanical, optical and magnetic properties. On the other hand, in the high-concentration limit (*ca.* 15–33%), the sample polarization becomes increasingly difficult and the electromechanical properties are degraded. Yet, these composites remain useful for their interesting mechanical actuating properties,[12] with the advantage that the mechano-electric coupling between the SCO phenomenon and the matrix gives rise to an electrical signal, which may be potentially useful for sensing and control purposes. Interestingly, in some favorable cases, we could even demonstrate an effective sum up of the pyroelectric response of the polymer and the piezoelectric response induced by the SCO filler. This result provides prospects for developing composite materials with enhanced thermal–electrical harvesting output.

Conflicts of interest

There are no conflicts to declare.

Acknowledgements

Financial support from the Federal University of Toulouse/Occitanie Région (PhD grant of MPB), the European Commission (H2020-MSCA-RISE-2016, SPINSWITCH, No. 734322) and the Agence Nationale de la Recherche (ANR-19-CE09-0008-01) is acknowledged.

Notes and references

1 *Energy Harvesting Technologies*, ed. S. Priya and D. J. Inman, Springer US, New York, 2009.
2 J.-H. Lee, J. Kim, T. Y. Kim, M. S. Al Hossain, S.-W. Kim and J. H. Kim, *J. Mater. Chem. A*, 2016, **4**, 7983.
3 H. Liu, J. Zhong, C. Lee, S.-W. Lee and L. Lin, *Appl. Phys. Rev.*, 2018, **5**, 041306.
4 M. Safaei, H. A. Sodano and S. R. Anton, *Smart Mater. Struct.*, 2019, **28**, 113001.
5 C. R. Bowen, J. Taylor, E. LeBoulbar, D. Zabek, A. Chauhan and R. Vaish, *Energy Environ. Sci.*, 2014, **7**, 3836.
6 A. Thakre, A. Kumar, H.-C. Song, D.-Y. Jeong and J. Ryu, *Sensors*, 2019, **19**, 2170.
7 S. Mishra, L. Unnikrishnan, S. K. Nayak and S. Mohanty, *Macromol. Mater. Eng.*, 2019, **304**, 1800463.
8 B. Gusarov, E. Gusarova, B. Viala, L. Gimeno, S. Boisseau, O. Cugat, E. Vandelle and B. Louison, *Sens. Actuators, A*, 2016, **243**, 175.

9 *Spin Crossover in Transition Metal Compounds I-III*, ed. P. Gütlich and H. A. Goodwin, Springer, Berlin, 2004, vol. 233–235.
10 P. Gütlich, A. Hauser and H. Spiering, *Angew. Chem., Int. Ed. Engl.*, 1994, **33**, 2024.
11 P. Guionneau, *Dalton Trans.*, 2014, **43**, 382.
12 S. Rat, M. Piedrahita-Bello, L. Salmon, G. Molnár, P. Demont and A. Bousseksou, *Adv. Mater.*, 2018, **30**, 1705275.
13 Y.-S. Koo and J. R. Galán-Mascarós, *Adv. Mater.*, 2014, **26**, 6785.
14 P. Martins, A. C. Lopes and S. Lanceros-Mendez, *Prog. Polym. Sci.*, 2014, **39**, 683.
15 G. Teyssèdre and C. Lacabanne, *Ferroelectrics*, 1995, **171**, 125.
16 M. Piedrahita-Bello, K. Ridier, M. Mikolasek, G. Molnár, W. Nicolazzi, L. Salmon and A. Bousseksou, *Chem. Commun.*, 2019, **55**, 4769.
17 S. Rat, K. Ridier, L. Vendier, G. Molnár, L. Salmon and A. Bousseksou, *CrystEngComm*, 2017, **19**, 3271.
18 I. Suleimanov, J. S. Costa, G. Molnár, L. Salmon, I. O. Fritsky and A. Bousseksou, *Fr.-Ukr. J. Chem.*, 2015, **3**, 66.
19 R. Gregorio, *J. Appl. Polym. Sci.*, 2006, **100**, 3272.
20 K. Tashiro and M. Kobayashi, *Polymer*, 1988, **29**, 426.
21 L. G. Lavrenova and O. G. Shakirova, *Eur. J. Inorg. Chem.*, 2013, 670.
22 M. D. Manrique-Juárez, I. Suleimanov, E. M. Hernández, L. Salmon, G. Molnár and A. Bousseksou, *Materials*, 2016, **9**, 537.
23 J. Clements, G. R. Davies and I. M. Ward, *Polymer*, 1992, **33**, 1623.
24 L. Stoleriu, P. Chakraborty, A. Hauser, A. Stancu and C. Enachescu, *Phys. Rev. B: Condens. Matter Mater. Phys.*, 2011, **84**, 134102.
25 T. H. L. Nguyen, L. Laffont, J.-F. Capsal, P.-J. Cottinet, A. Lonjon, E. Dantras and C. Lacabanne, *Mater. Chem. Phys.*, 2015, **153**, 195.
26 A. Grosjean, P. Négrier, P. Bordet, C. Etrillard, D. Mondieig, S. Pechev, E. Lebraud, J.-F. Létard and P. Guionneau, *Eur. J. Inorg. Chem.*, 2013, 796.

Electronic Supplementary Material (ESI) for Journal of Materials Chemistry C.

Mechano-electric coupling in PVDF/spin crossover nano-composites

Mario Piedrahita-Bello,[a] Baptiste Martin,[b] Lionel Salmon,*[a] Gábor Molnár,[a] Philippe Demont[b] and Azzedine Bousseksou*[a]

[a]LCC, CNRS & University of Toulouse (UPS, INPT), 205 route de Narbonne, 31077 Toulouse, France. E-mail: azzedine.bousseksou@lcc-toulouse.fr

[b] CIRIMAT, CNRS & University of Toulouse (UPS, INPT), 118 Route de Narbonne, 31062 Toulouse. E-mail: philippe.demont@univ-tlse3.fr

Table S1: Elemental analyses of SCO complexes

SCO sample	%C (found)	%C (calc)	%H (found)	%H (calc)	%N (found)	%N (calc)	%B (found)	%B (calc)	%Fe (found)	%Fe (calc)
1	19.3	19.5	1.99	2.81	35.6	34.9	3.1	3.07	15.7	15.2
2	18.8	18.6	2.16	2.91	33.4	33.6	3.23	3.21	14.8	14.4
3	18.2	18.3	1.6	2.84	31.8	32.6	3.45	3.42	14.1	14.2
4	20.3	20.6	2.08	3.13	32.9	34.1	2.71	2.85	15.2	14.8
5	24.3	24.2	3.91	4.4	41.7	42.3				

Figure S1: SEM images of the composite **1a** cross-section.

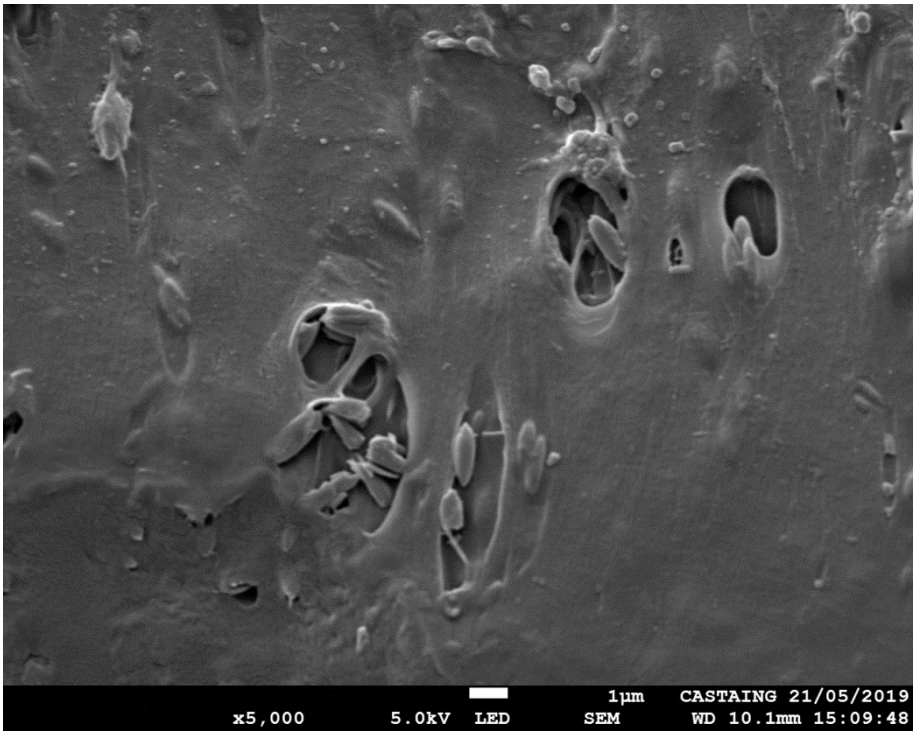

Figure S2: SEM coupled EDX analysis of two randomly selected areas for composite **1a**

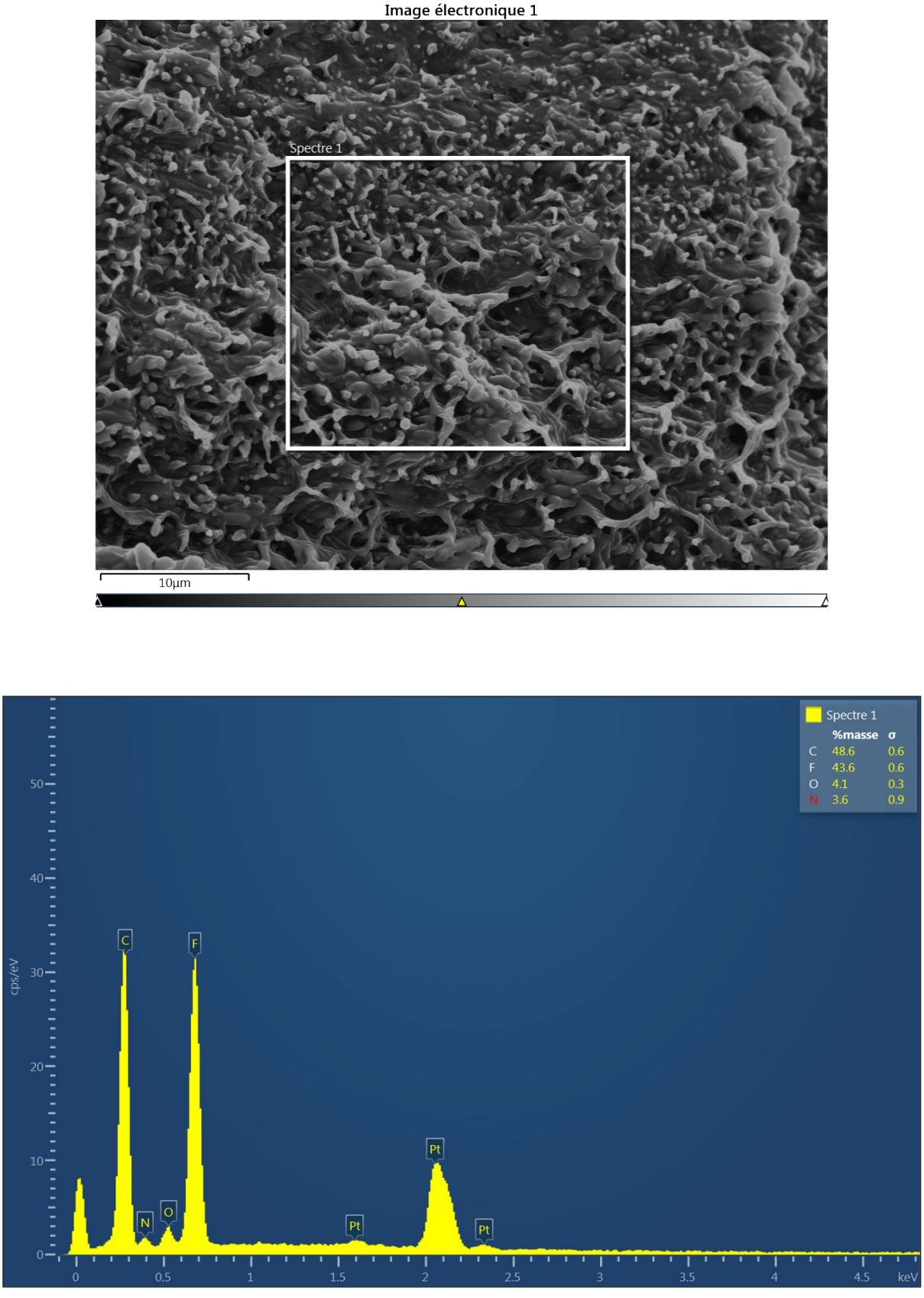

Image électronique 2

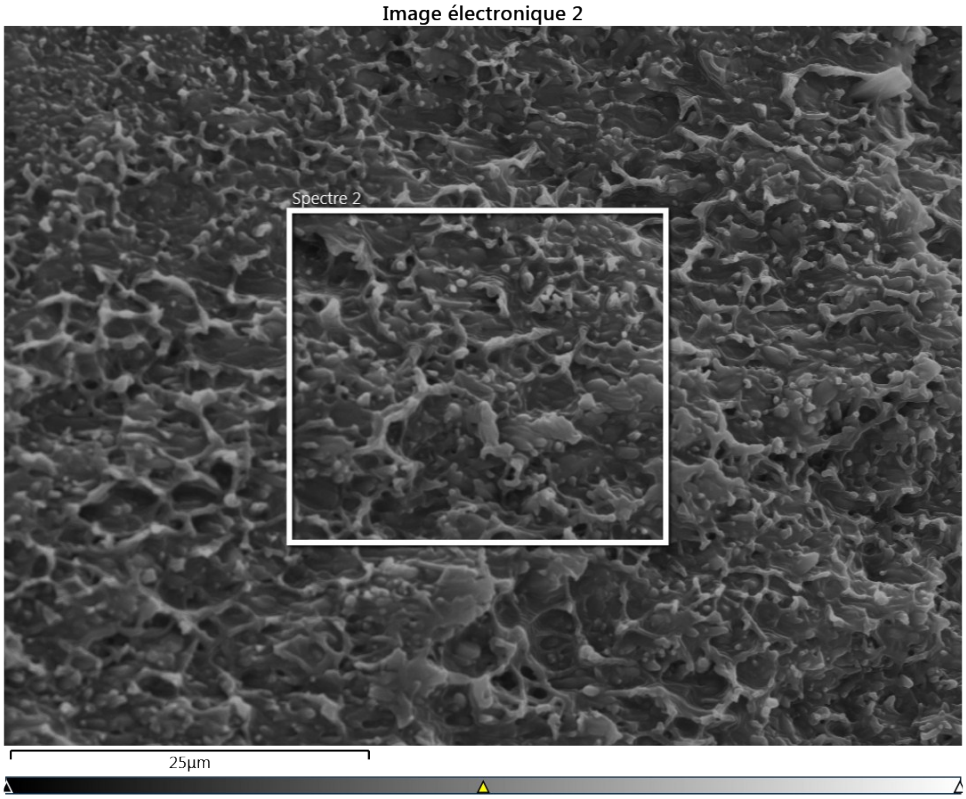

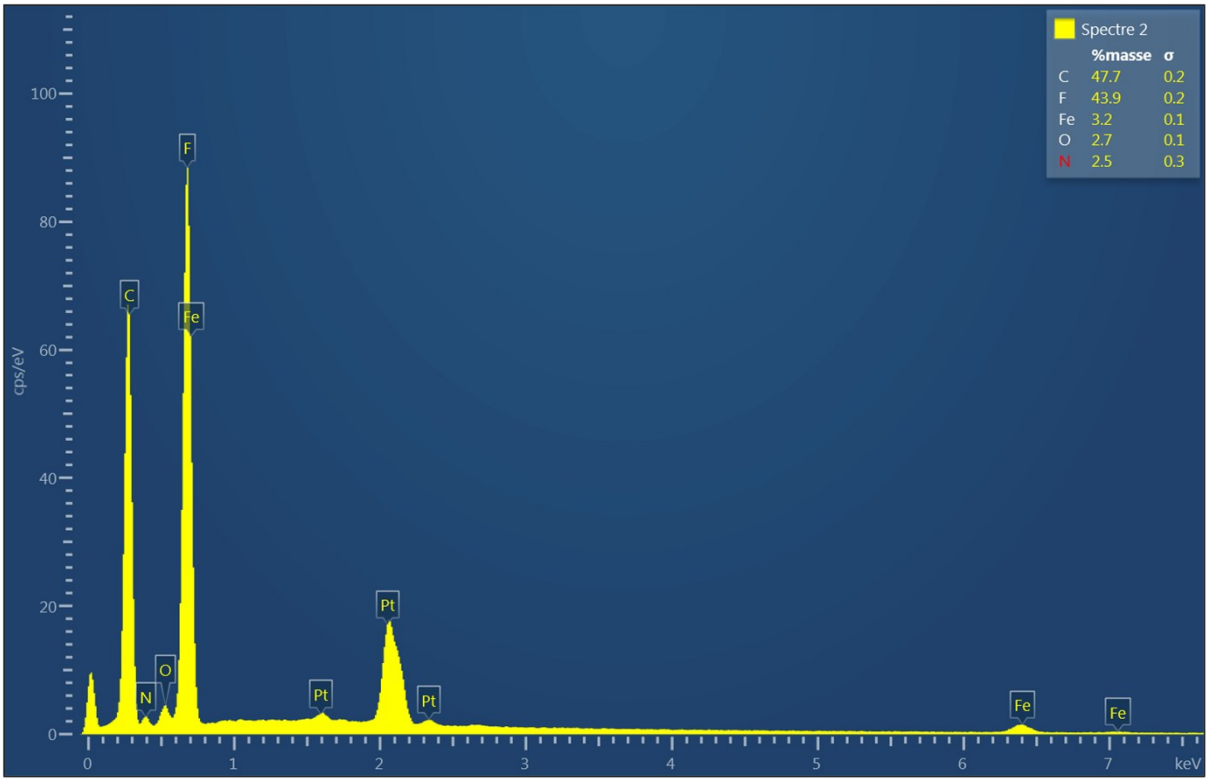

Figure S3: SEM images of the composite **4a** cross-section.

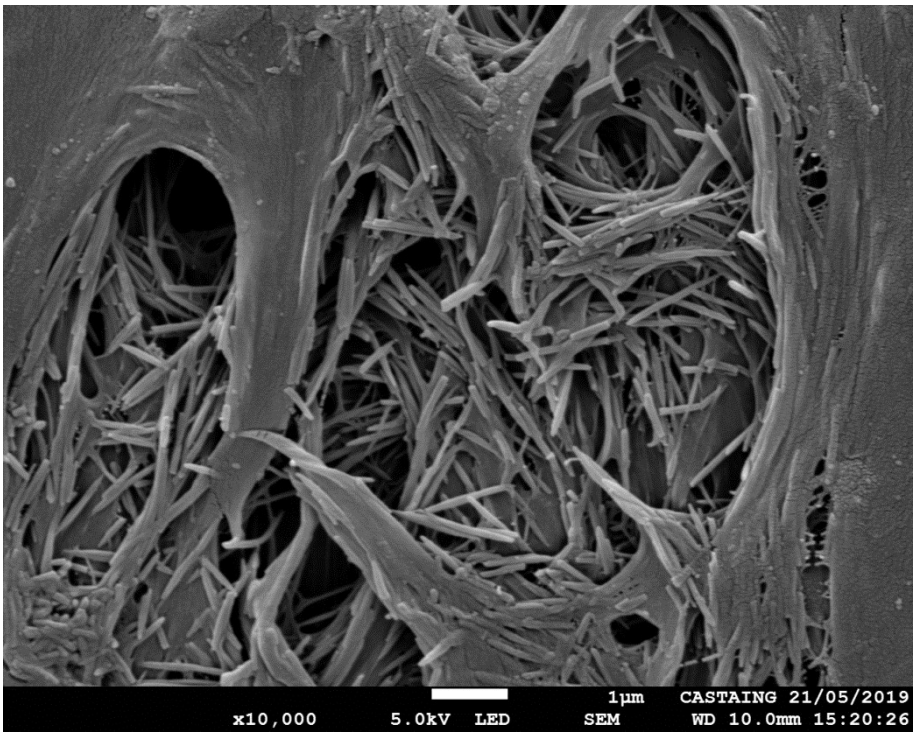

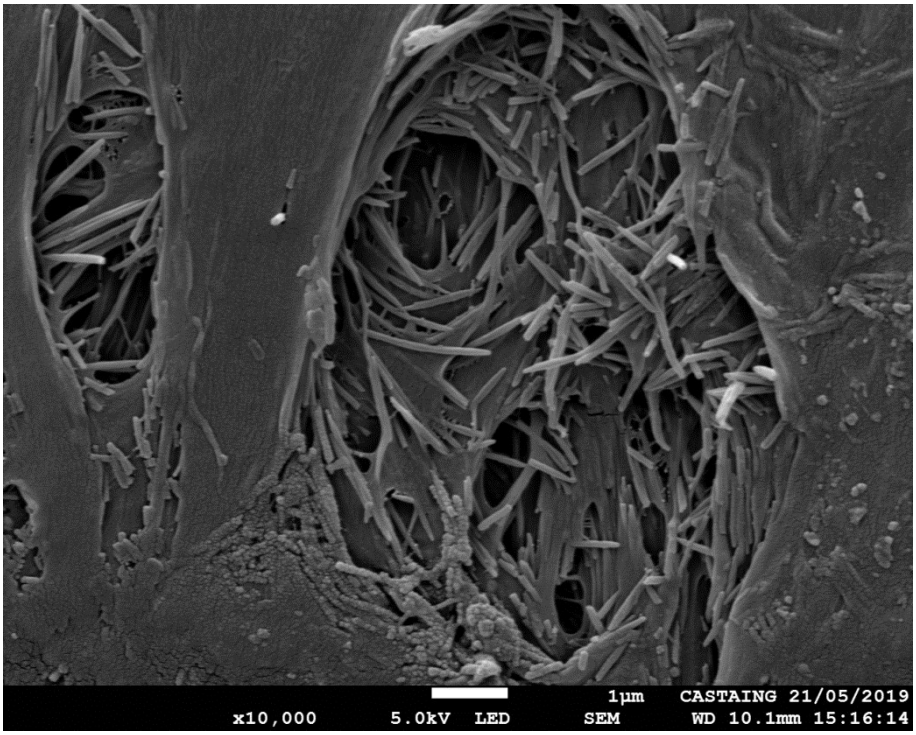

Figure S4: SEM coupled EDX analysis of two randomly selected areas for composite **4a**.

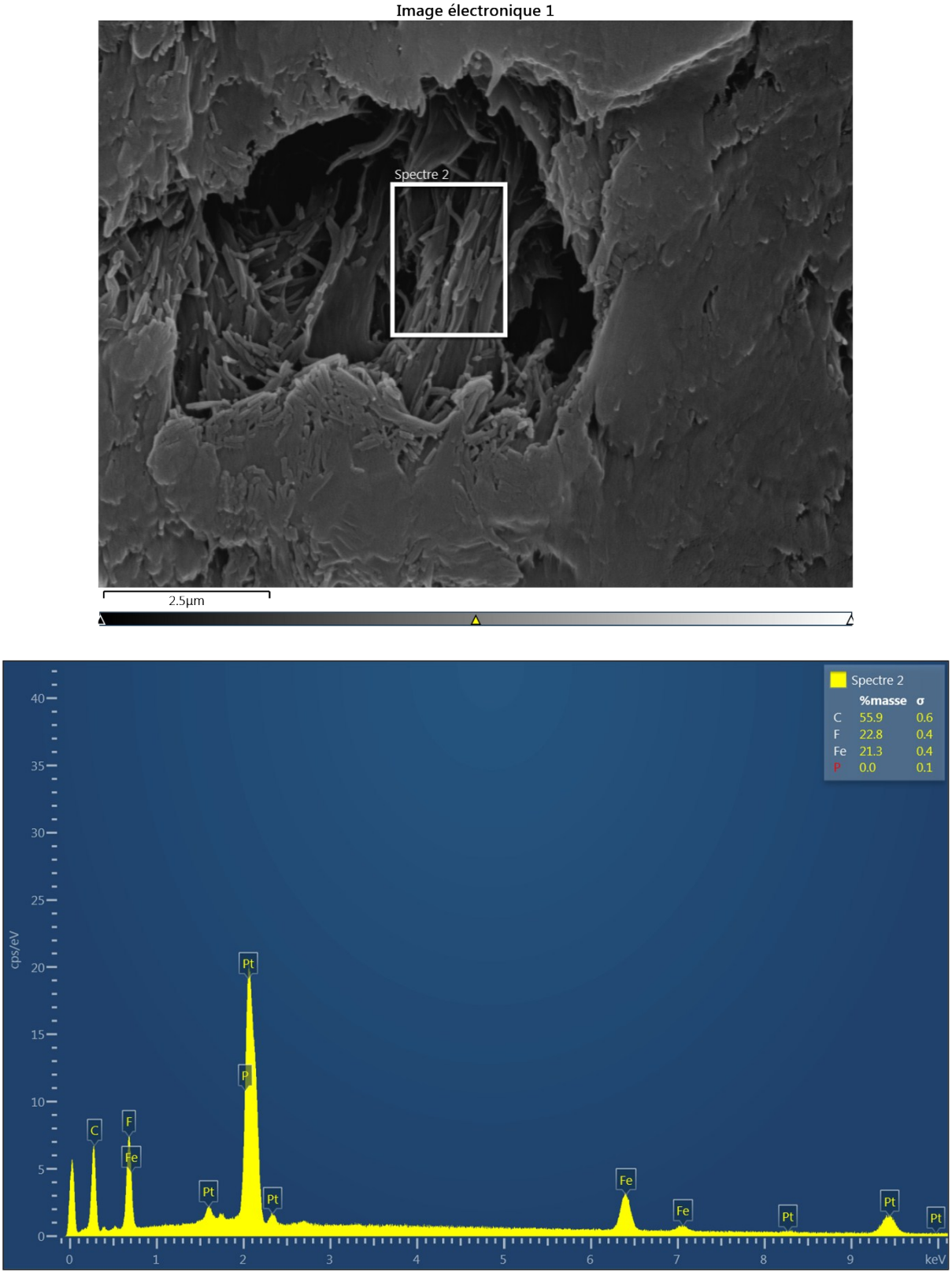

Image électronique 2

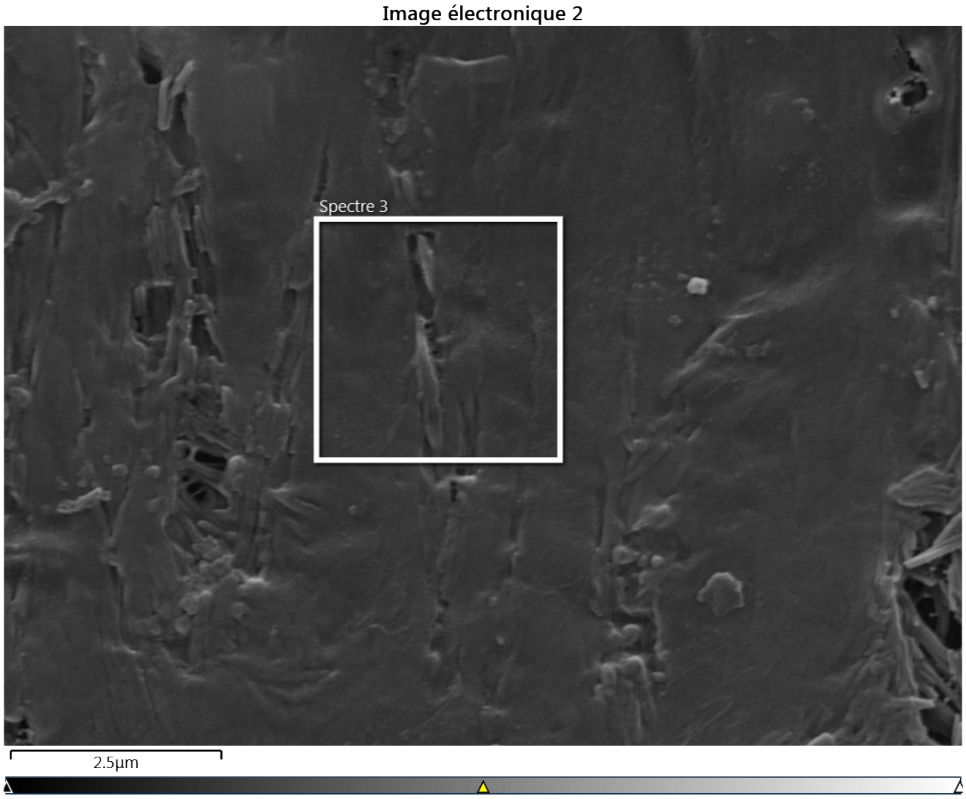

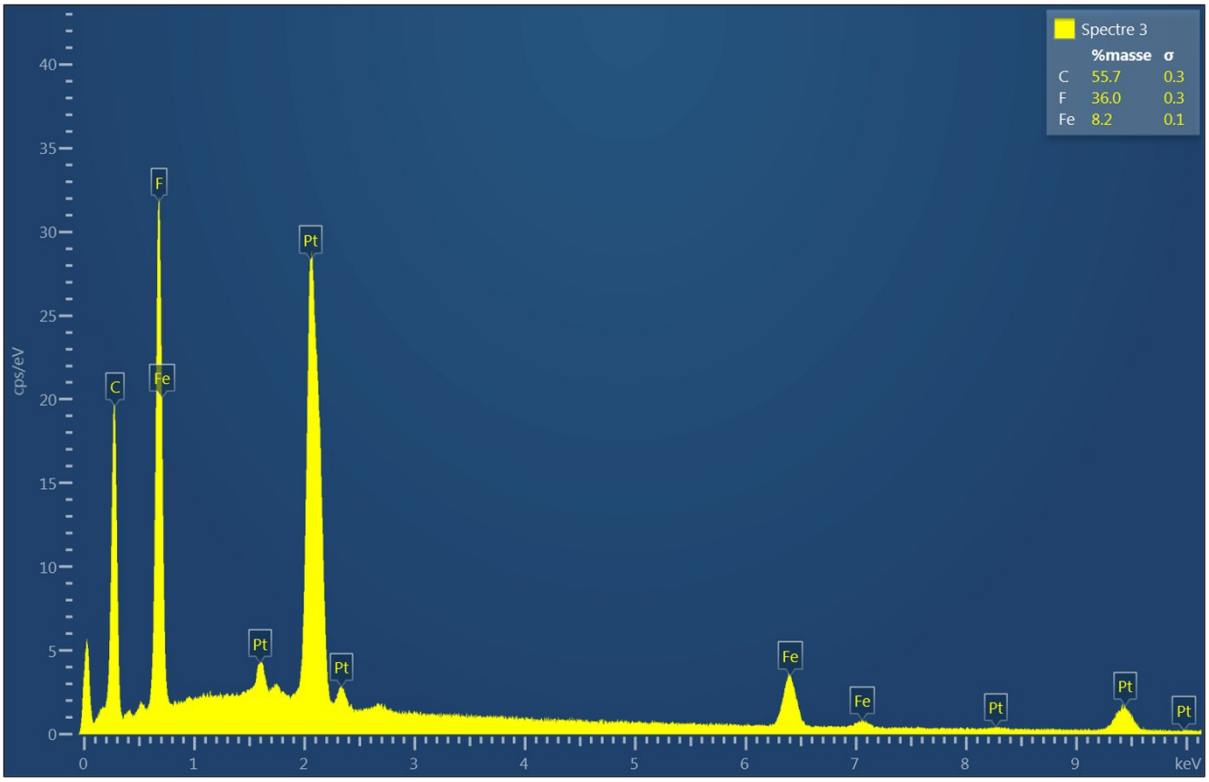

Figure S5: SEM images of the composite **5c** cross-section

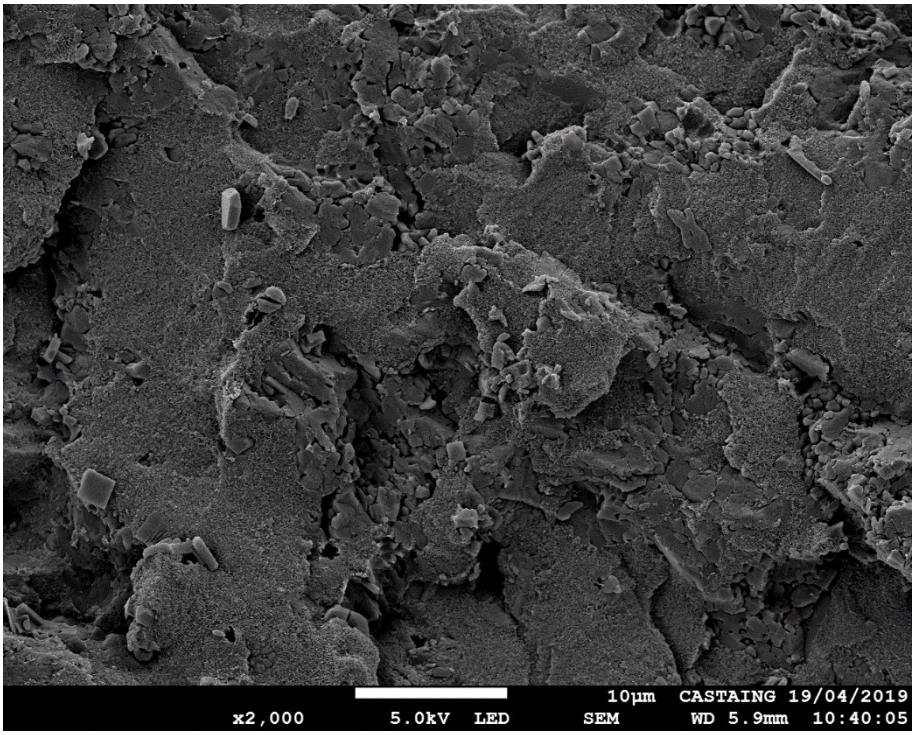

Figure S6: SEM coupled EDX analysis for composite **5c**

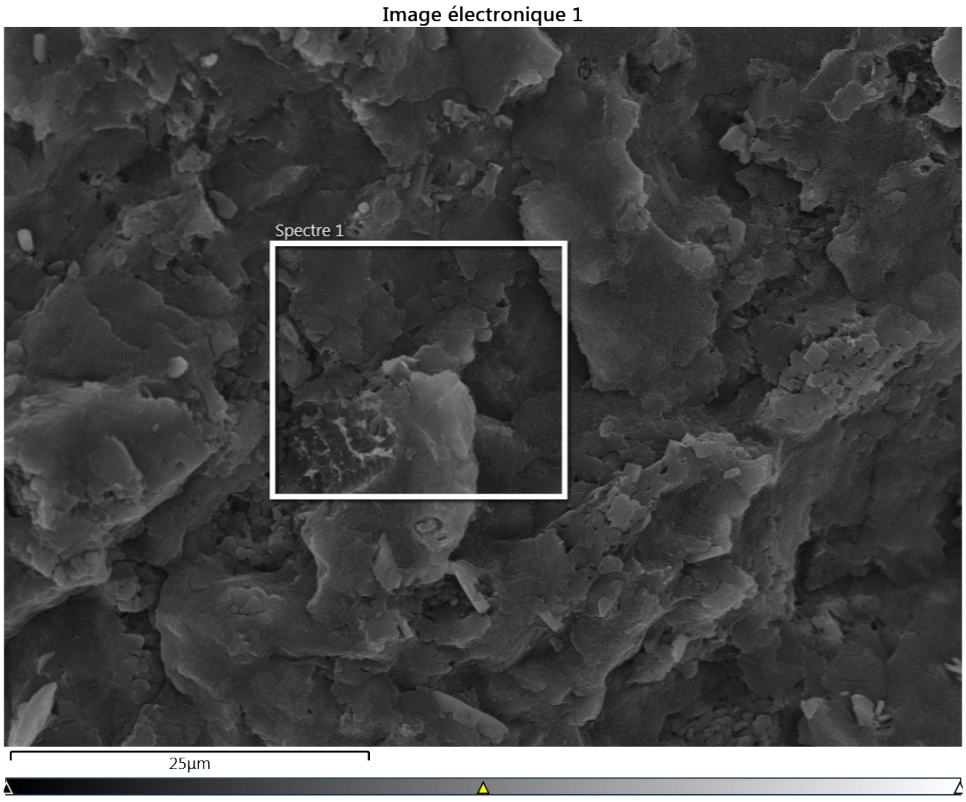

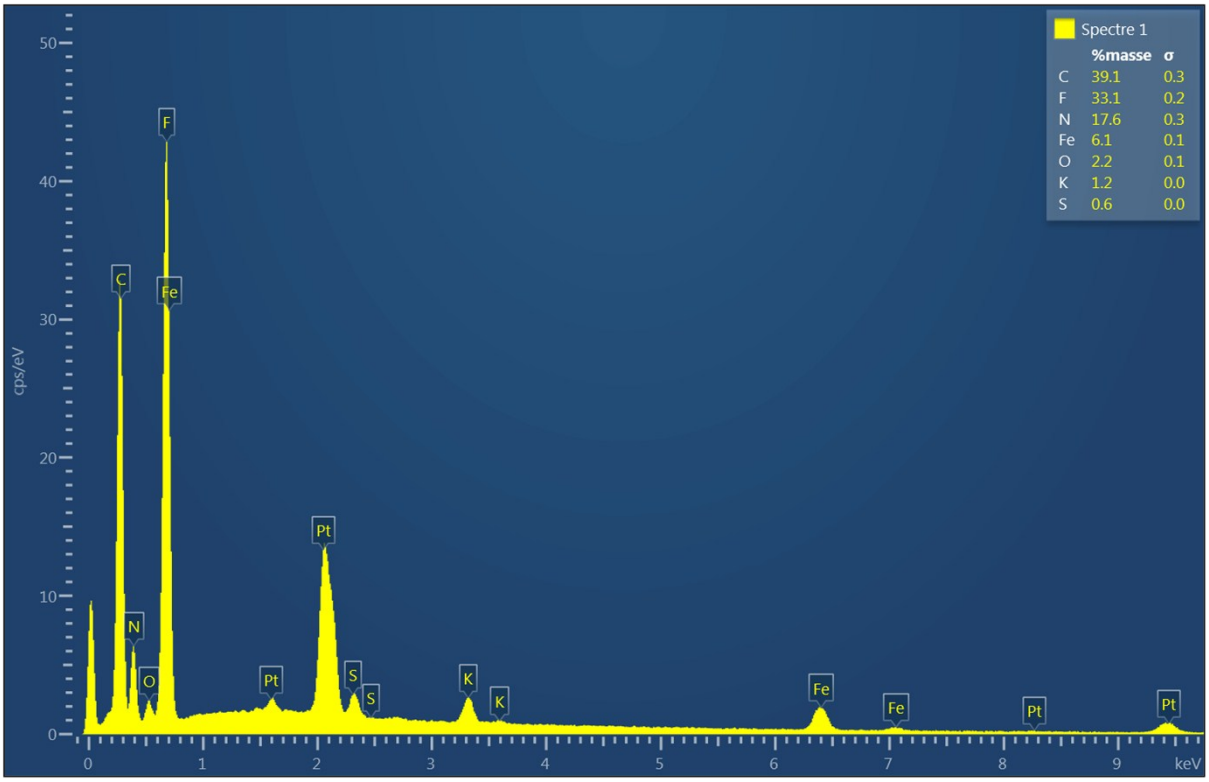

Figure S7: Powder XRD of the different composite **5a-5e** recorded at room temperature

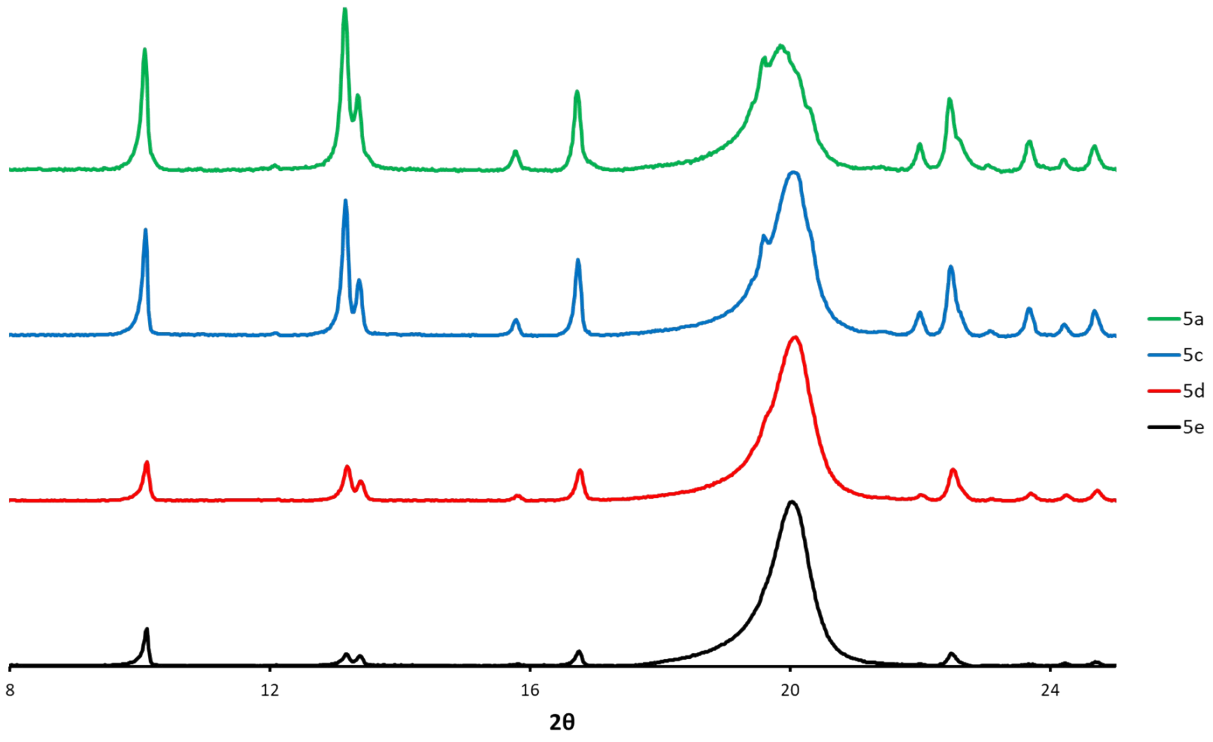

Figure S8: DSC Measurements for the composite materials and the pure copolymers

1a – 15% Triazole Mix Bulk PVDF-TrFE - 75-25:

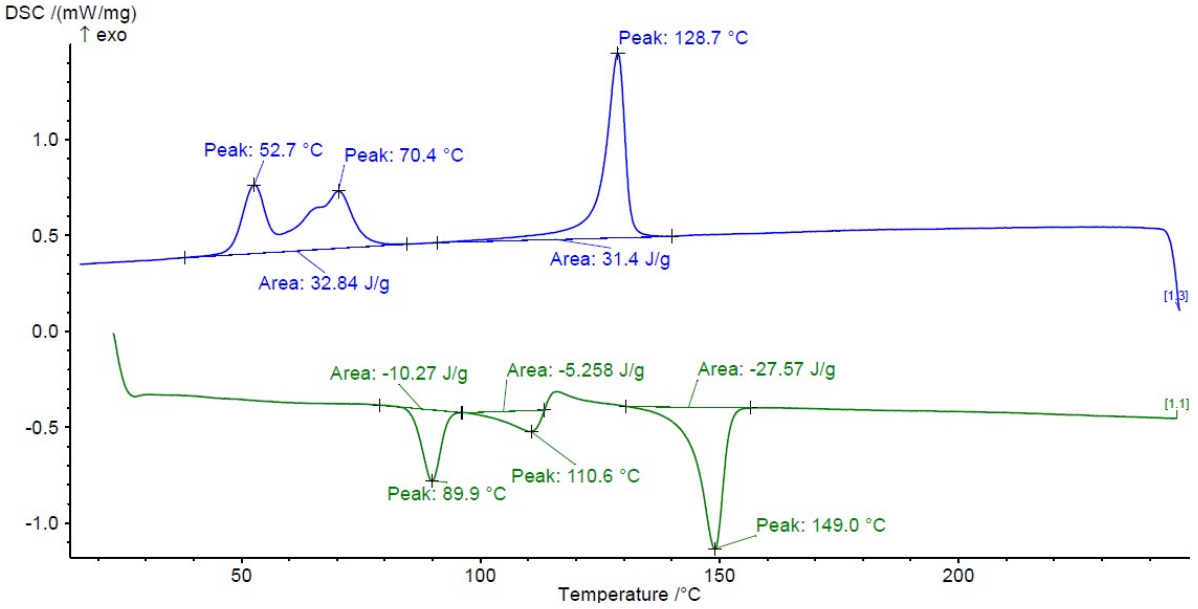

3a – 15% Triazole Mix Particles PVDF-TrFE – 75-25:

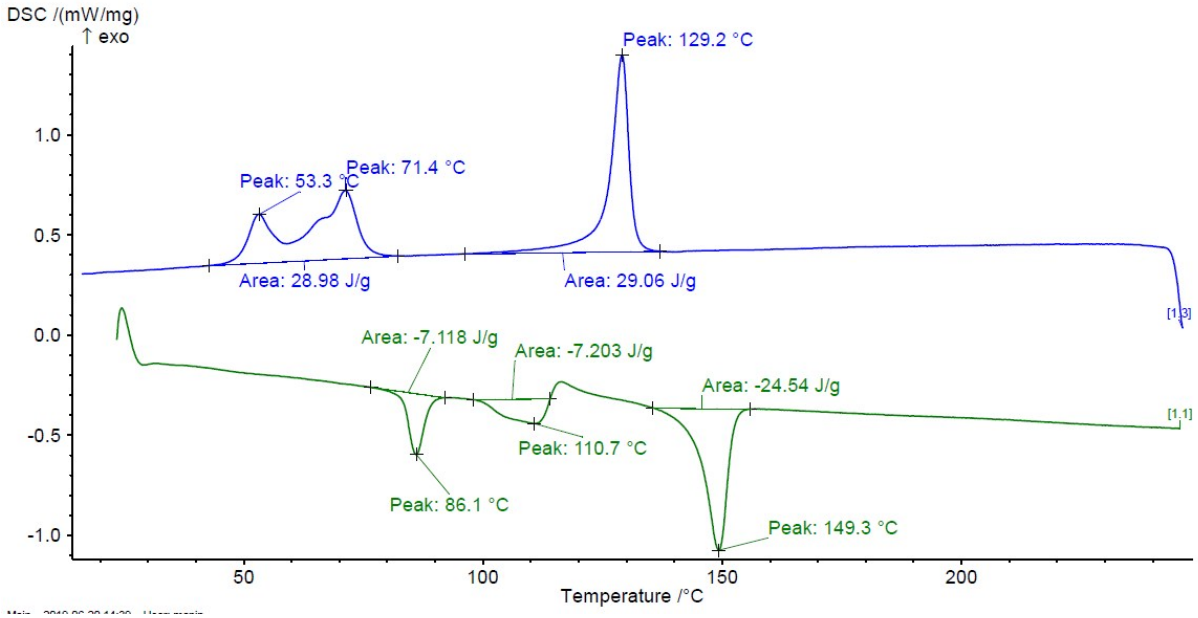

4a – 15% Triazole Mix 2µm Rods PVDF-TrFE – 75-25:

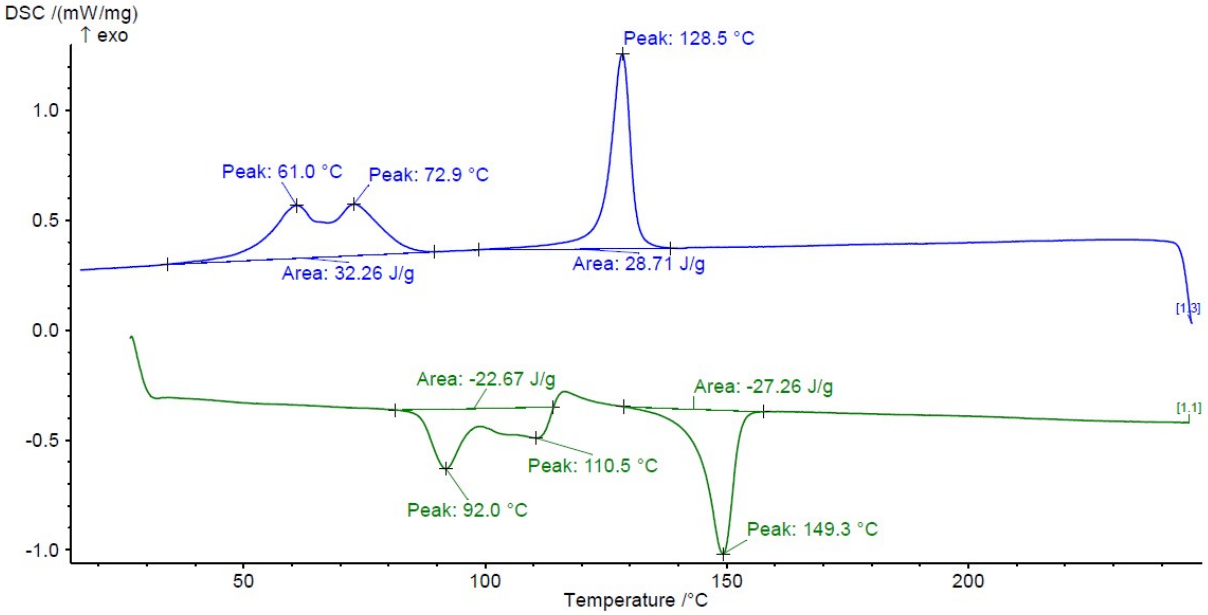

5a – 33% Triazolyl Borate PVDF-TrFE – 75-25:

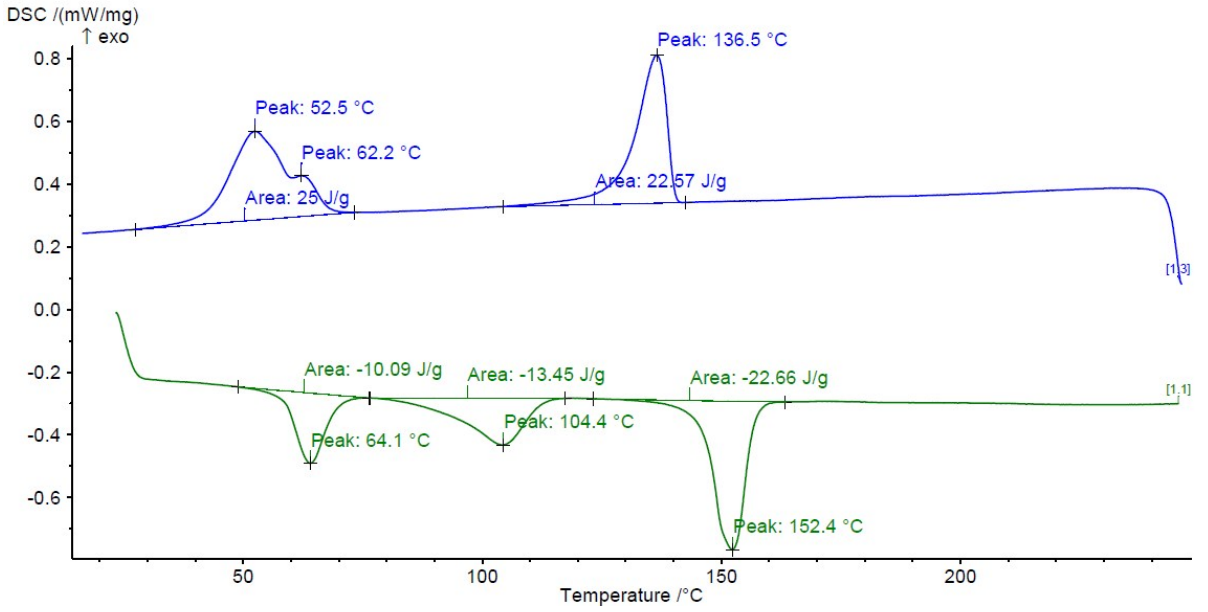

5b – 25% Triazolyl Borate PVDF-TrFE – 70-30:

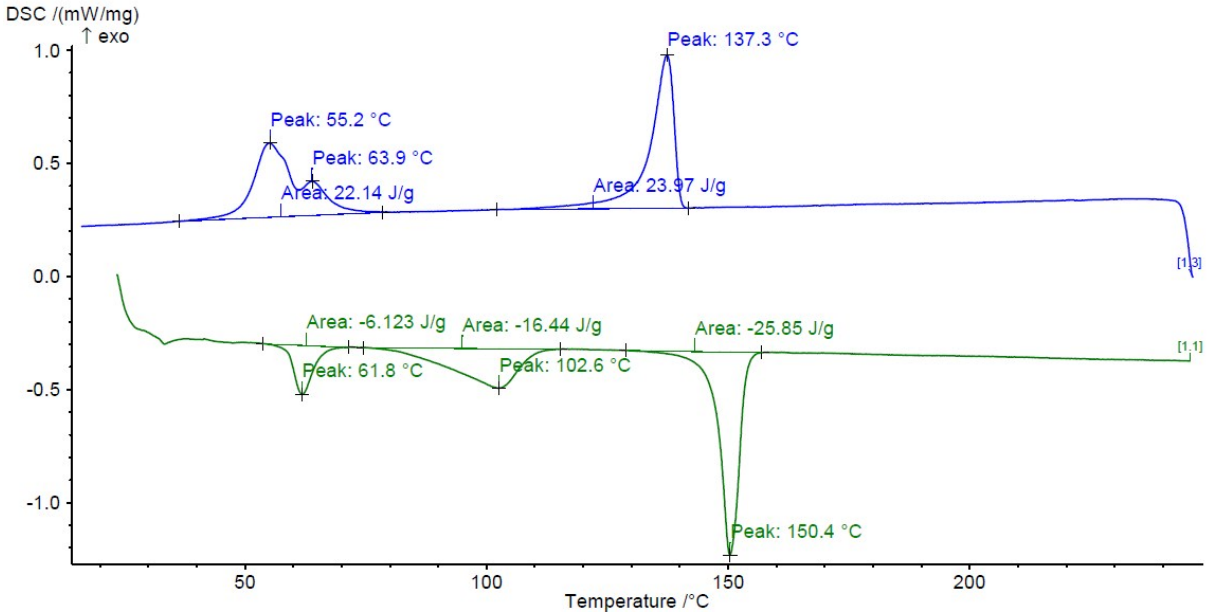

5c - 25% Triazolyl Borate PVDF-TrFE – 75-25:

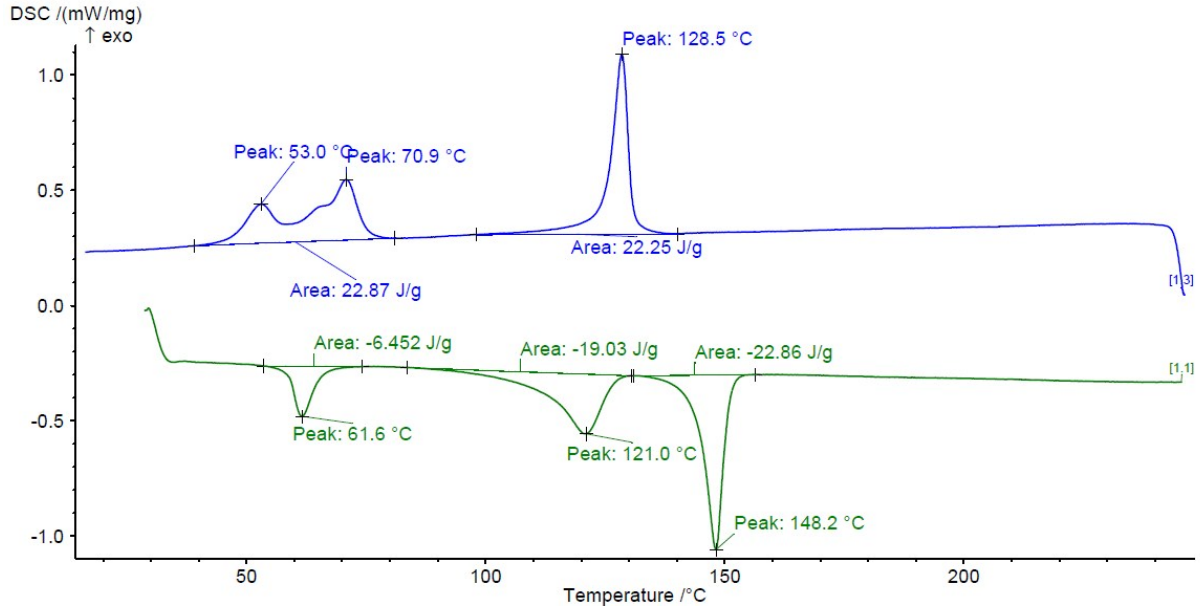

5d – 15% Triazolyl Borate PVDF-TrFE – 75-25:

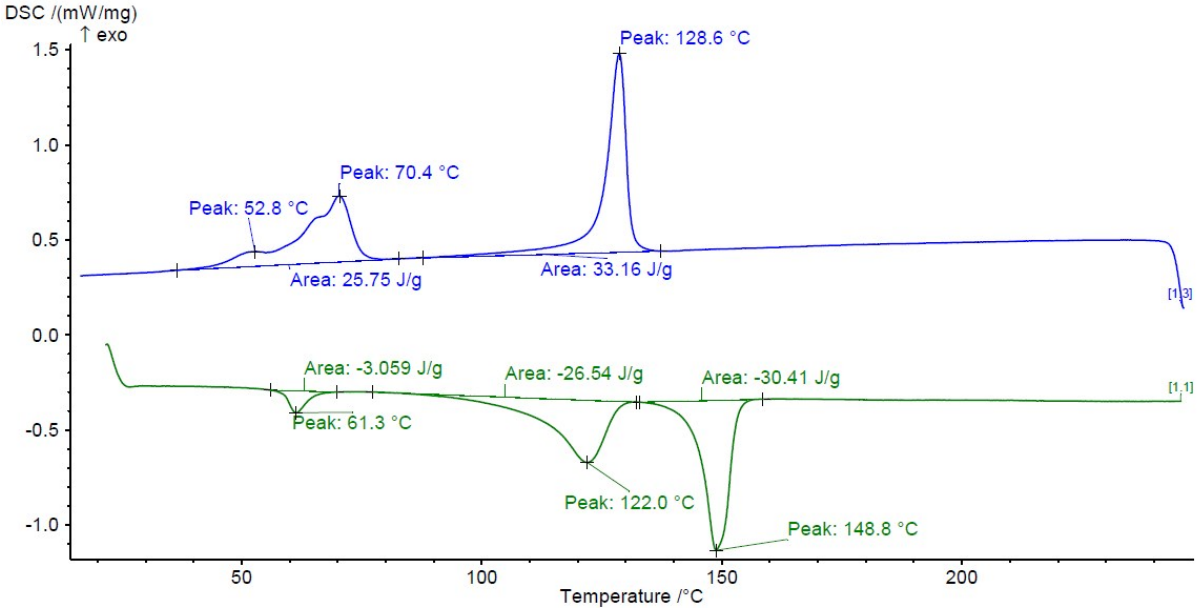

5e –5% Triazolyl Borate PVDF-TrFE – 75-25:

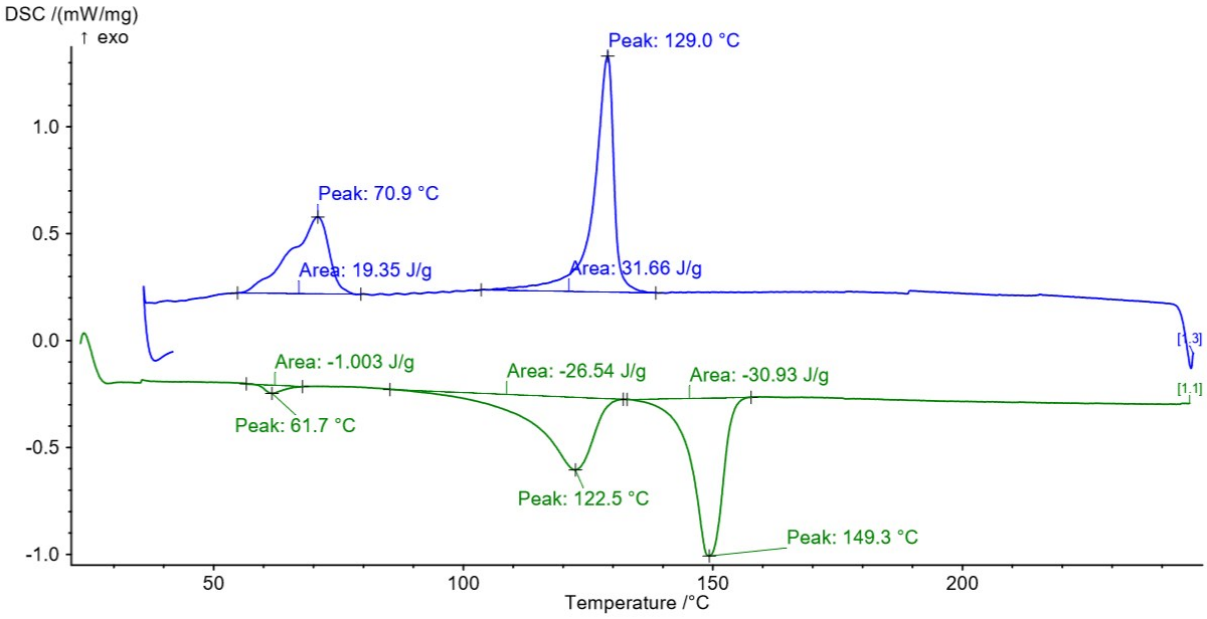

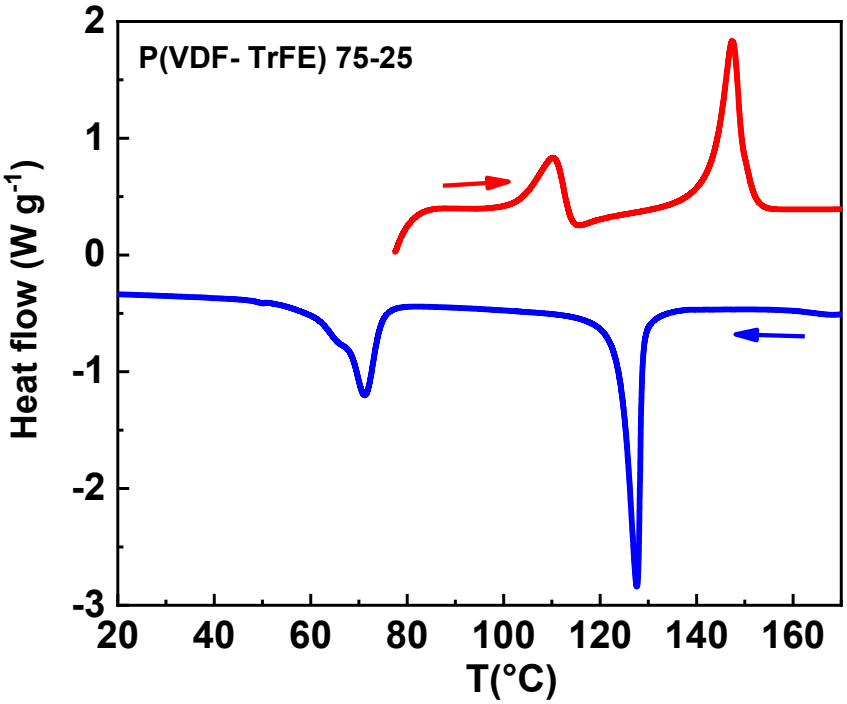
P(VDF- TrFE) 75-25
Heat flow (W g-1)
T(°C)
2
1
0
-1
-2
-3
20
40
60
80
100
120
140
160

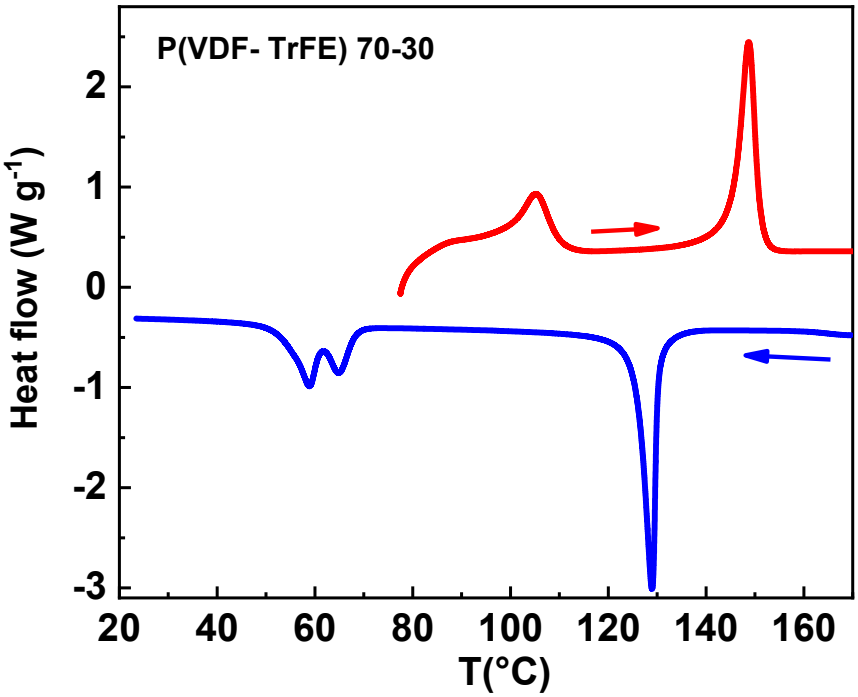
P(VDF- TrFE) 70-30
Heat flow (W g-1)
T(°C)
2
1
0
-1
-2
-3
20
40
60
80
100
120
140
160

Figure S9: Variable temperature optical reflectivity measurement of the different SCO powder samples.

Reflectivity of the 2nd thermal cycle of the bulk and particles used in the synthesis of composites **1** and **3** respectively.

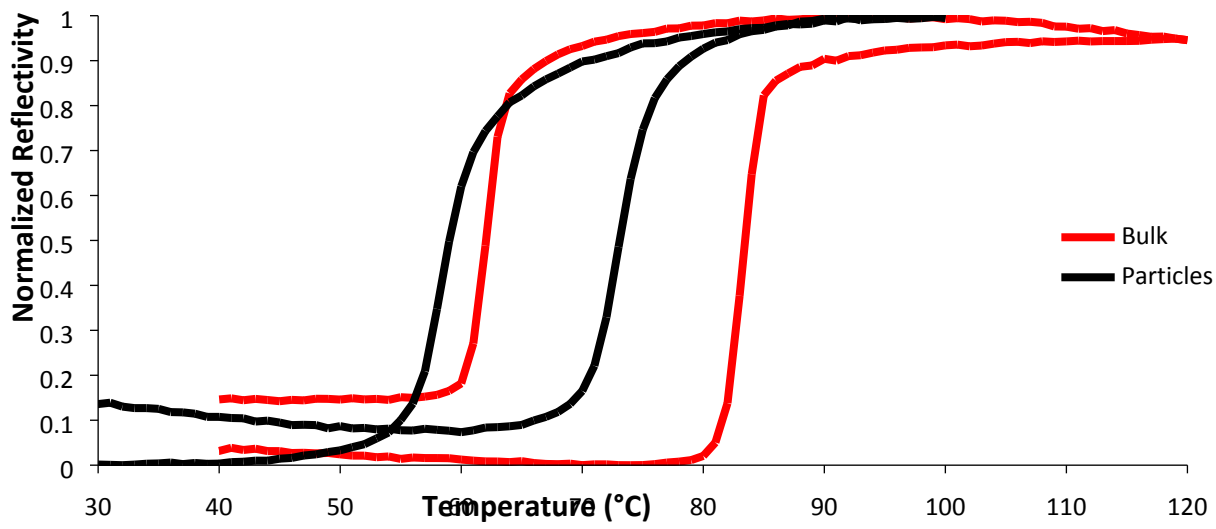

Reflectivity Measurement of the 2 um particles used in the synthesis of composite **4**

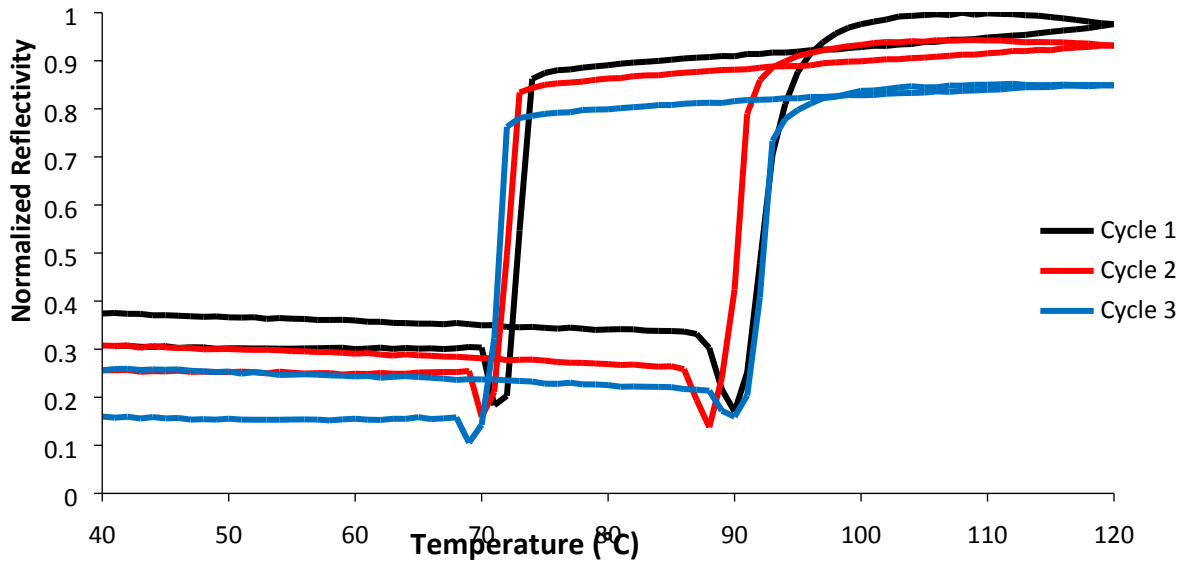

Figure S10: Variable temperature optical reflectivity measurement of the P(VDF-TrFE)/SCO composite

Reflectivity Measurement of Composite **1a**

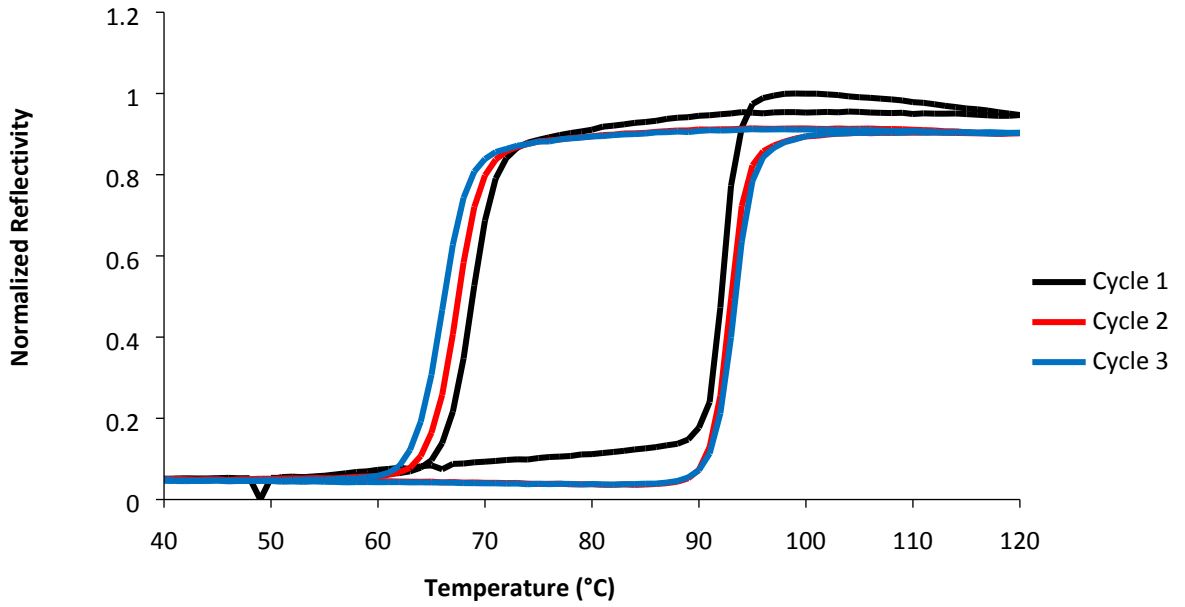

Reflectivity Measurement of Composite **3a**

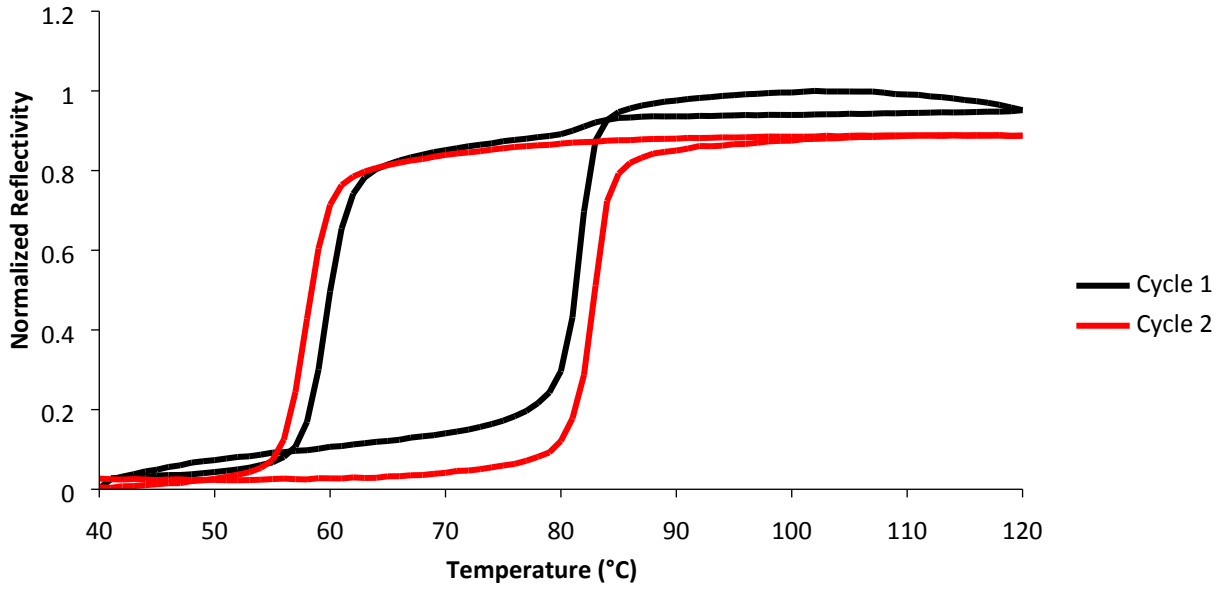

Reflectivity Measurement of Composite **4a**

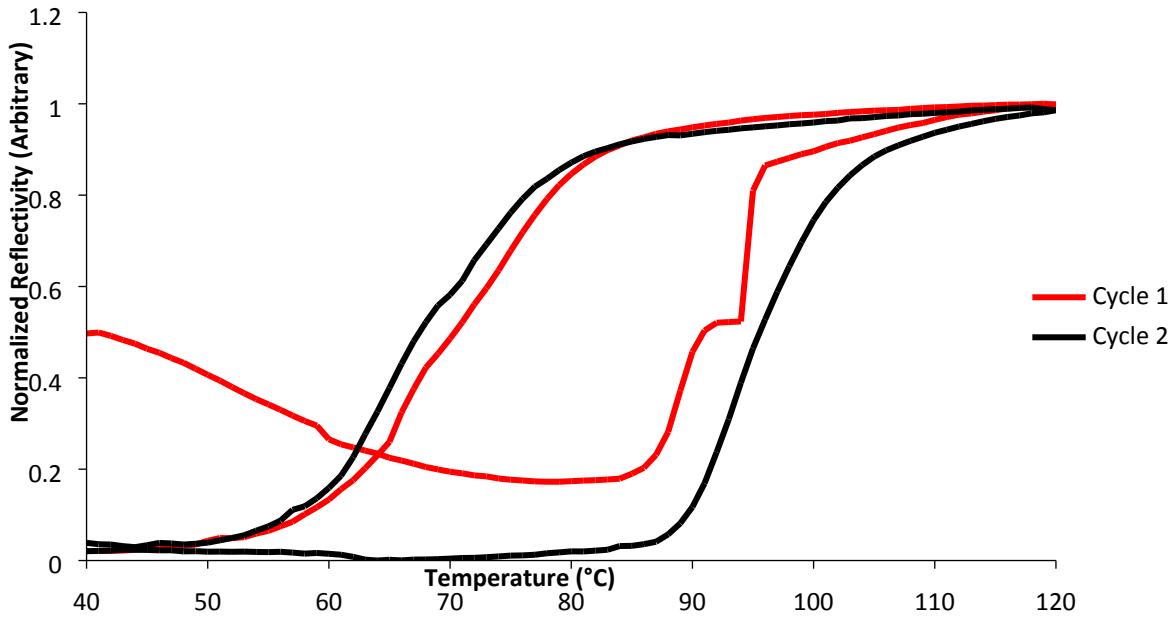

Reflectivity Measurement of Composite **5a**

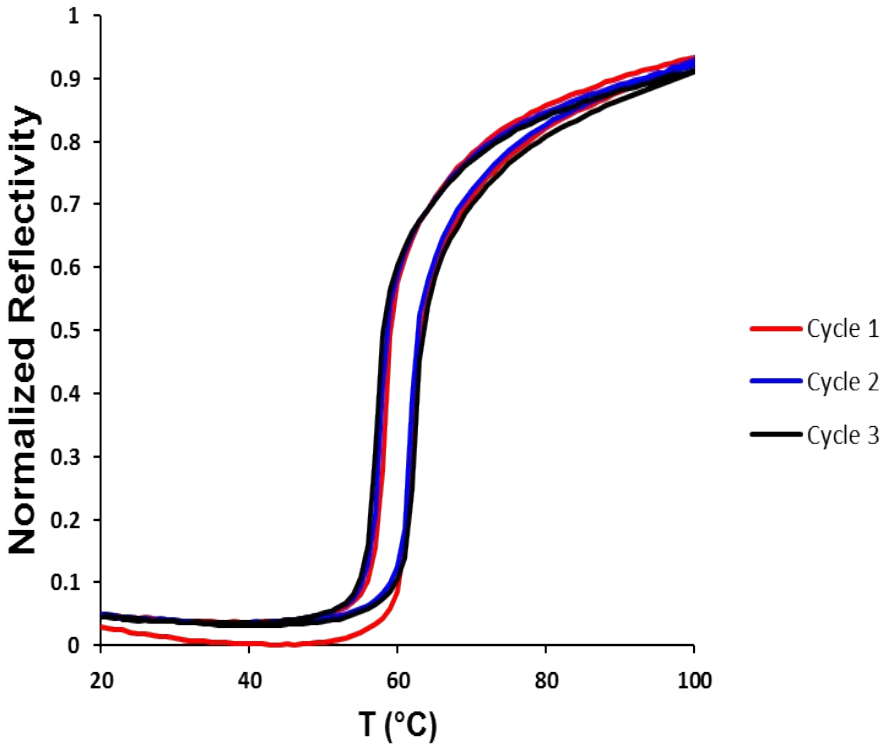

Figure S11: Pyroelectric discharge cycle for a depolarized and repolarized composite **1a**.

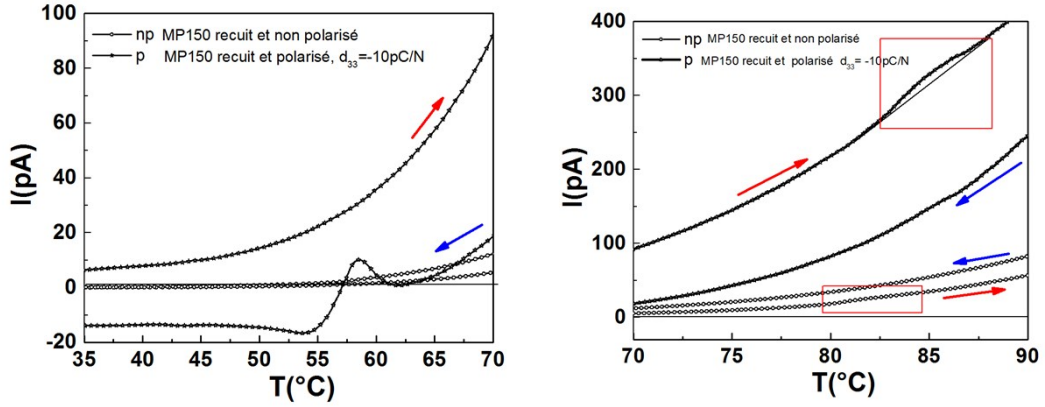

Figure S12: Pyroelectric discharge cycle for composite **2a** with different polarization intensities:

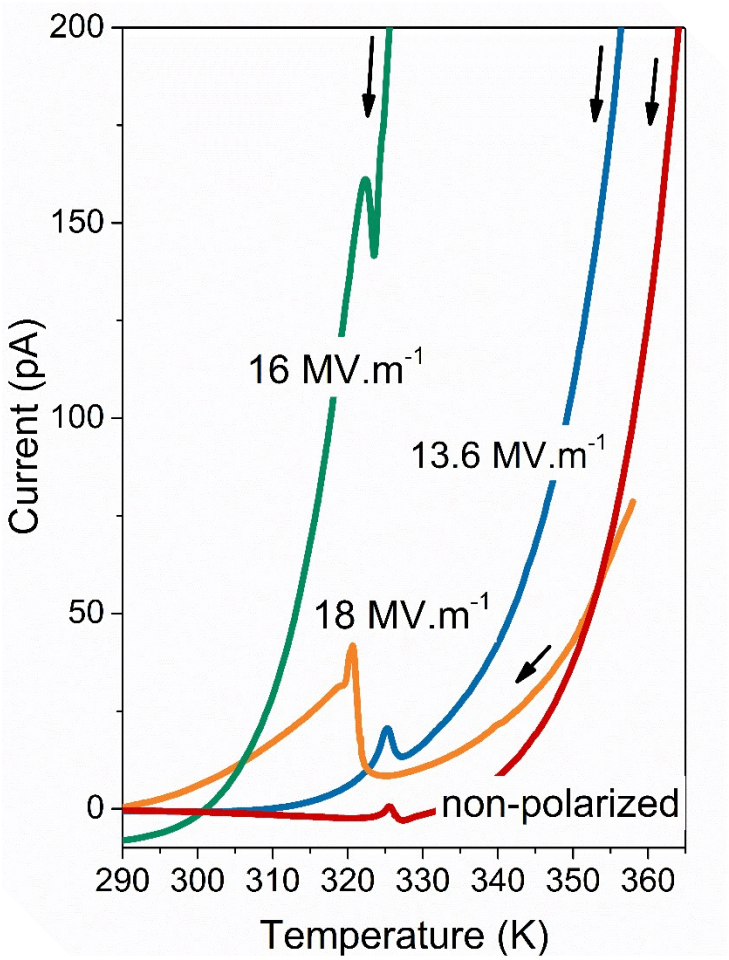

Figure S13. Pyroelectric discharge cycle for a polarized composite **3a**.

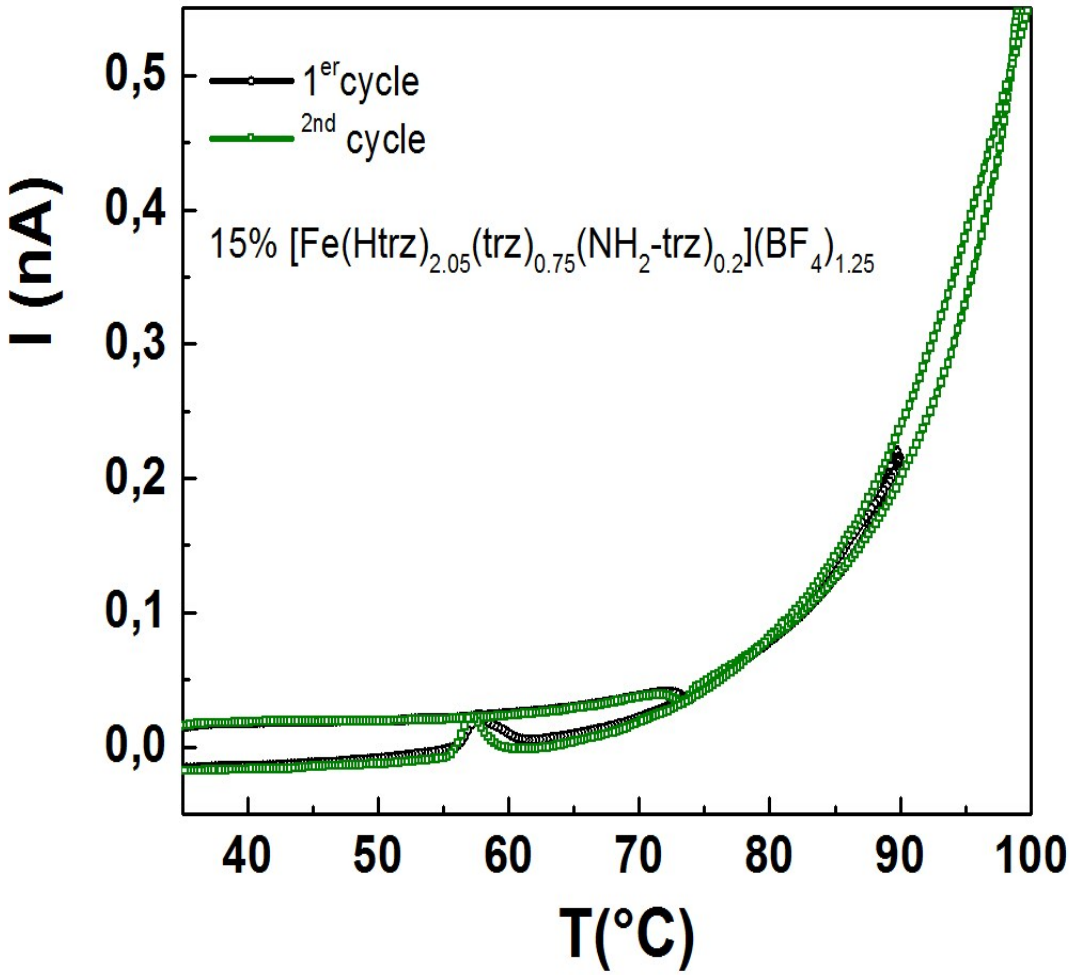

Figure S14. Pyroelectric discharge cycle for a polarized composite **4a**.

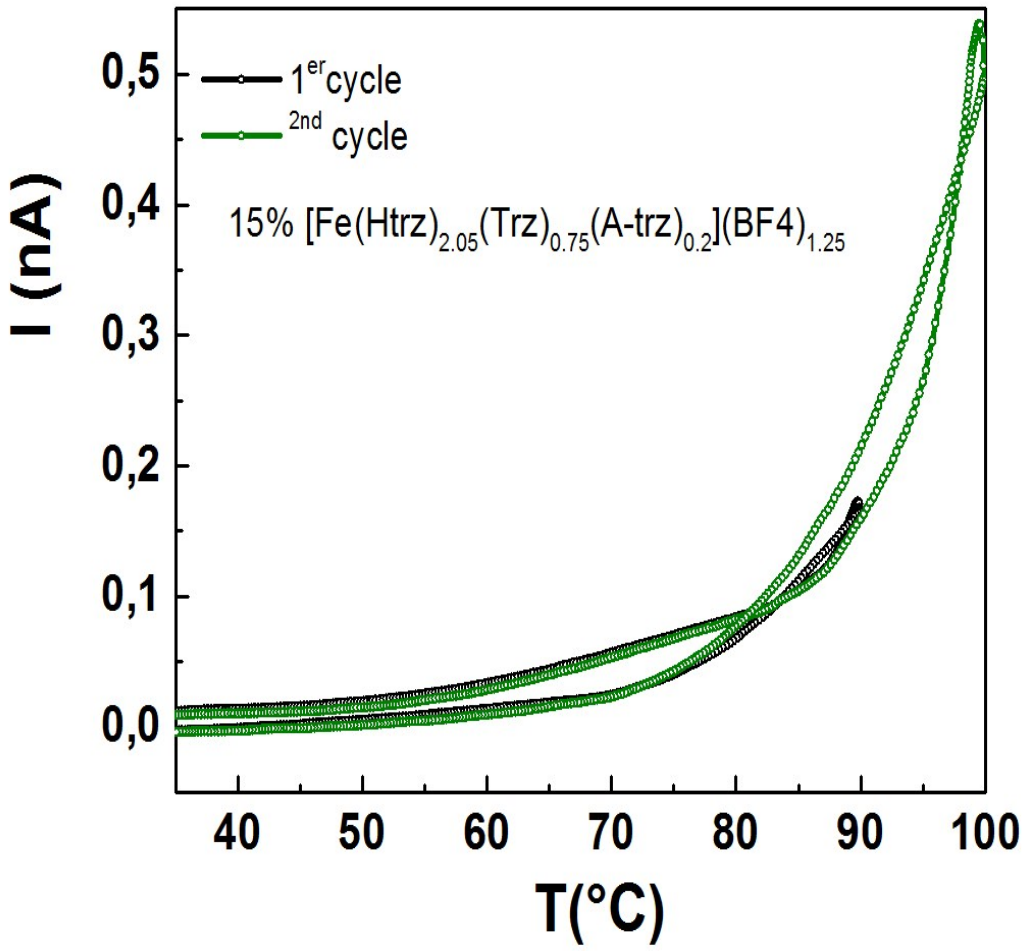

Figure S15. Pyroelectric discharge cycle for a polarized composite **5a**

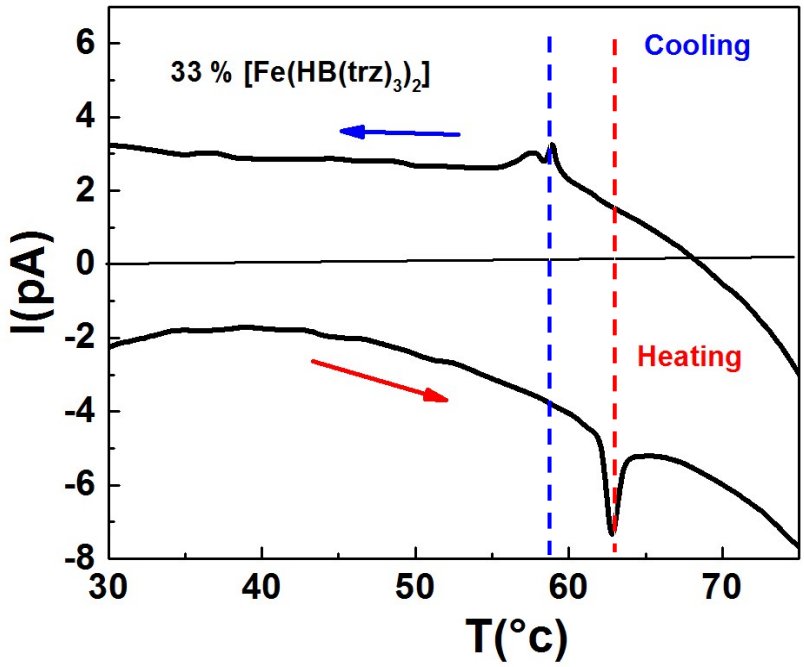

Figure S16. Pyroelectric discharge cycle for a polarized composite **5b**

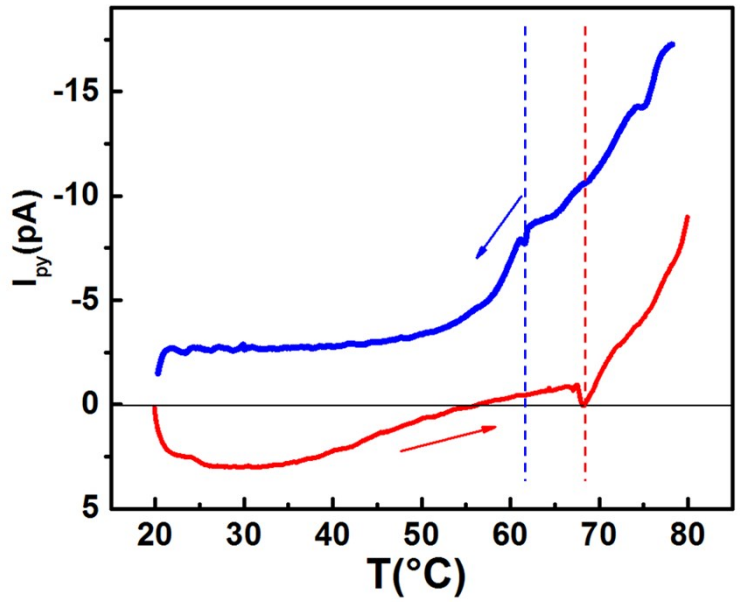

Figure S17. Pyroelectric discharge cycle for a polarized composite **5c**

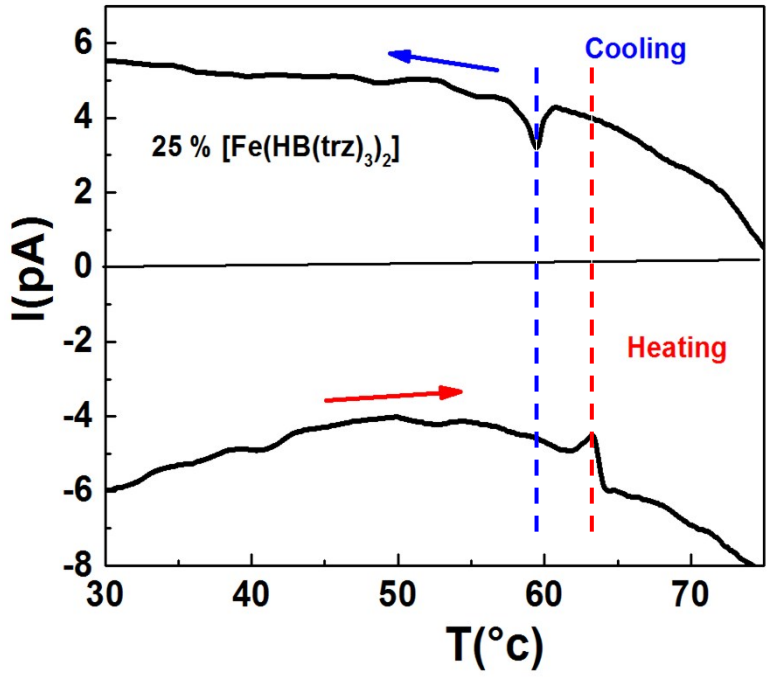

Figure S18. Pyroelectric discharge cycle for a nonpolarized Composite **5d**. Dotted lines indicate the discharge peak temperatures for cooling (left) and heating (right).

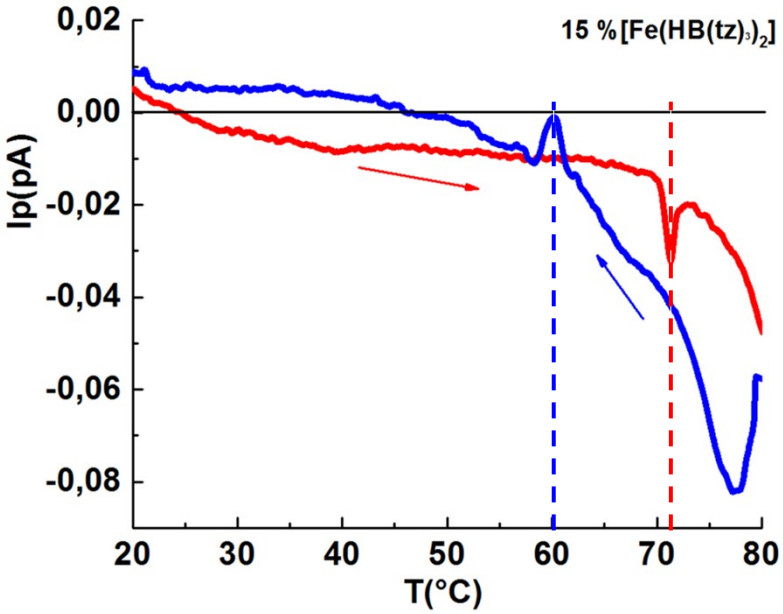

Figure S19. Pyroelectric discharge cycle for a polarized composite **5d**

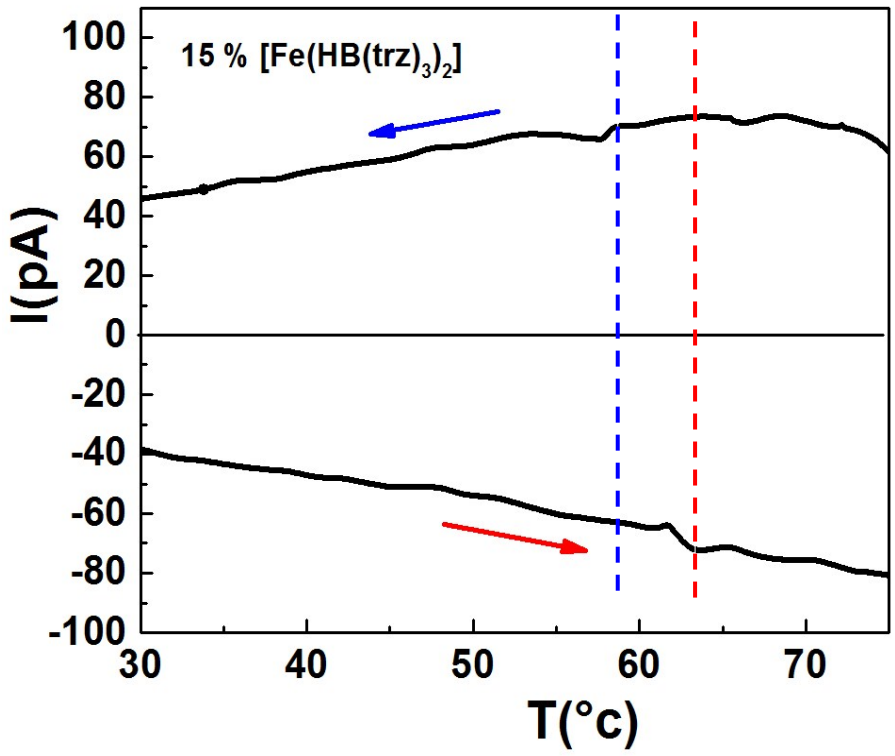

Figure S20. Pyroelectric discharge cycle for a polarized composite **5e**

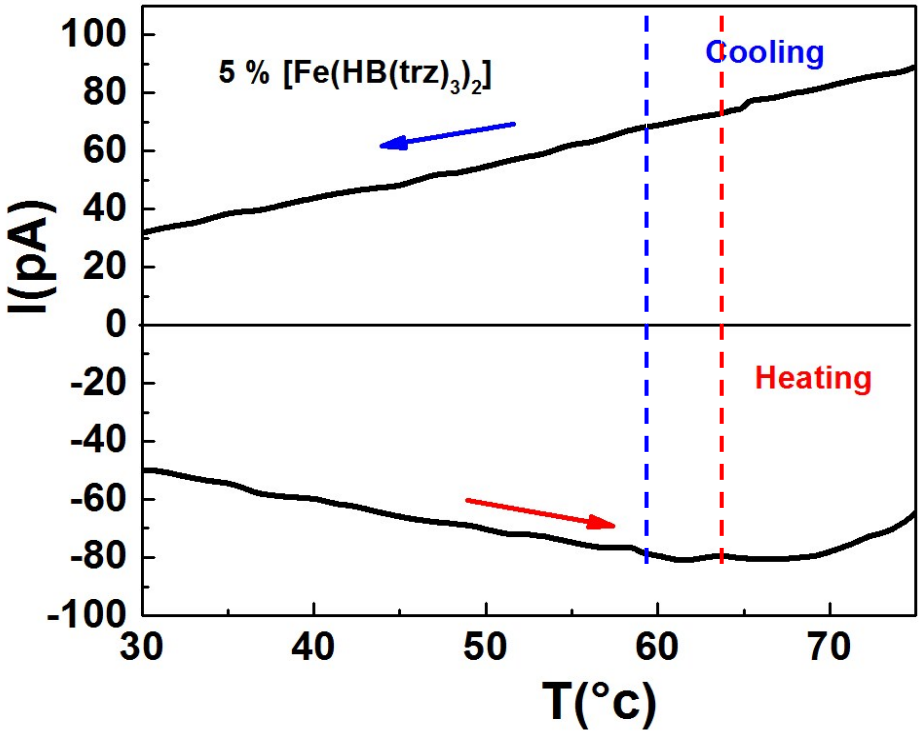

Figure S21. Pyroelectric discharge cycle for polarized composite **5a-5e**

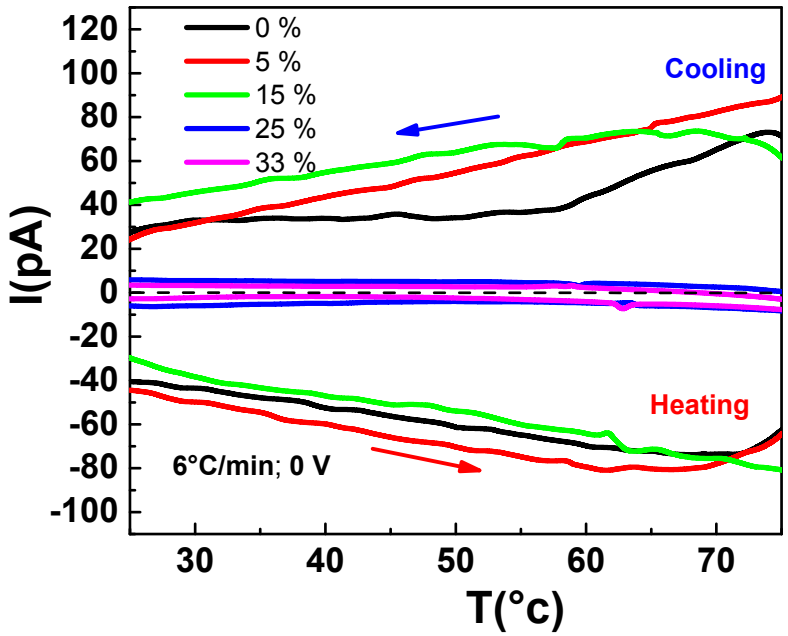

Figure S22. Pyroelectric discharge cycle for composite **5c** in two different orientations at two different speeds.

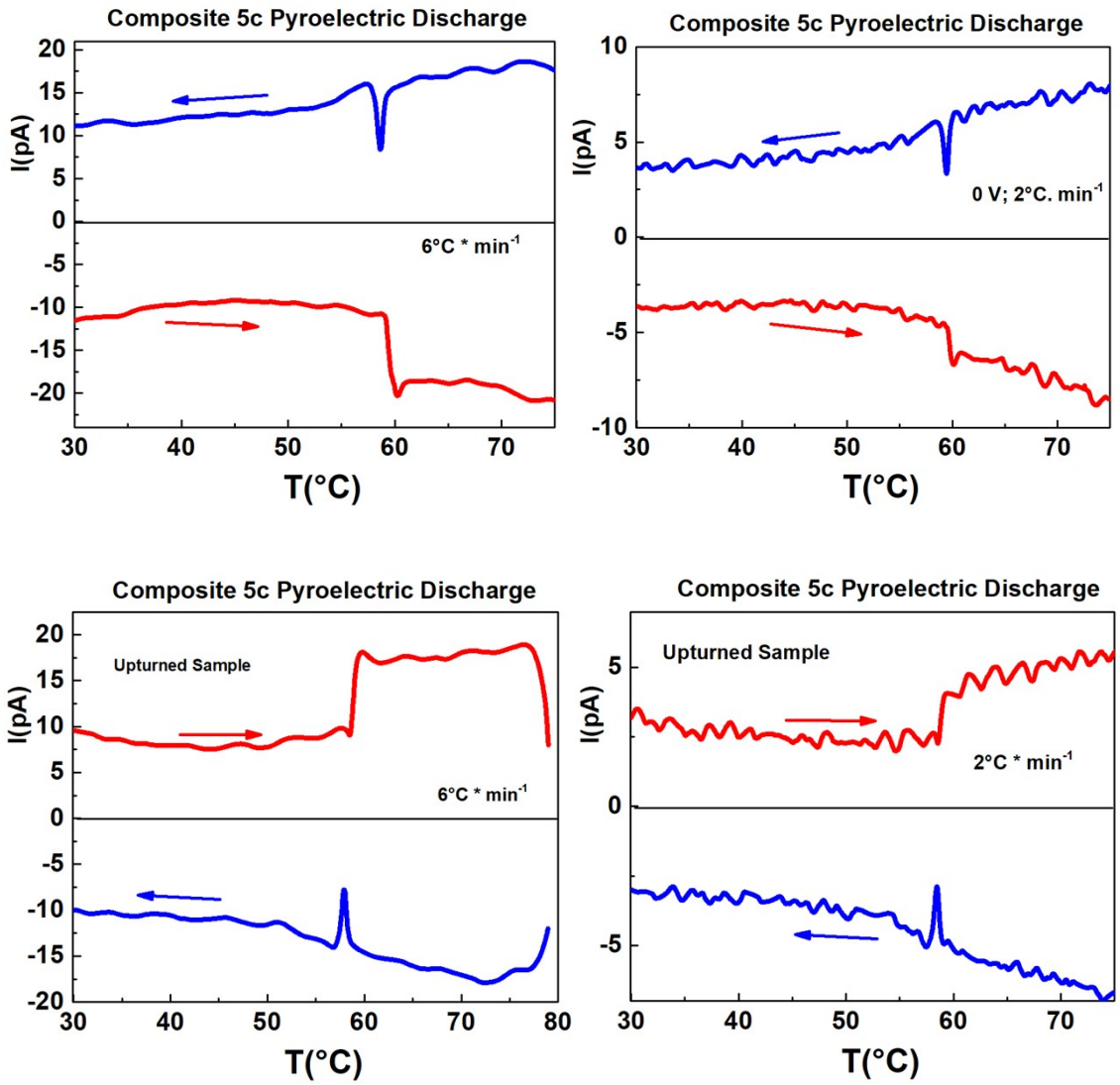

Figure S23: Temperature-dependent Permittivity measurement of sample 5c.